Single-Photon Emitters in Silicon for Quantum Technology

Towards Revealing the Nature of Recently Observed Quantum Emitters

Sindre Ludvigsen Tømta

Thesis submitted for the degree of
Master of Science: Material Science for Energy and Nanotechnology
60 credits

Department of Physics
Faculty of mathematics and natural sciences

UNIVERSITY OF OSLO

Spring 2021

Single-Photon Emitters in Silicon for Quantum Technology

Towards Revealing the Nature of Recently Observed Quantum Emitters

Sindre Ludvigsen Tømta

© 2021 Sindre Ludvigsen Tømta

Single-Photon Emitters in Silicon for Quantum Technology

http://www.duo.uio.no/

Printed: Reprosentralen, University of Oslo

Abstract

During WW2, Alan Turing and his team of clever codebreakers worked on cracking the encrypted German transmissions to turn the tide of war. The result brought into this world the basic principles of the first computer. Since then the technology have evolved tremendously and the processing power of the worlds computers is growing exponentially. The next revolution in computers is underway with the introduction of quantum computers which at present are performing at extremely low temperatures. Research on materials which may allow room temperature quantum supremacy is booming, including the exploration of optical qubits. Light sources emitting single-photons on-demand are at the kernel of other quantum technologies too, such as quantum communications and quantum networks. For practical purposes, the ideal single-photon source must exhibit high efficiency, room temperature functionality, compatibility with present day integrated circuits and telecom wavelength operation. Very recently single-photon emission was demonstrated from certain defects in silicon, in particular from the G center. Discovering other defects may assist the quantum computer revolution using silicon as a building block; capitalizing on high integration of silicon in the electronics industry.

This thesis studies the photoluminescence (PL) signals of potential single-photon emitters in silicon produced by irradiation with 1.8 MeV protons in range of fluences from 5E10 to 5E16. Both n- and p-type Si wafers were used in an attempt to discover whether the defects are associated with the dopants. Cryogenic condition (4K) PL was employed for identification of the irradiation-induced defects. The PL probing depth was optimized to match the projected range of ions by using 405 nm wavelength cw-laser as an excitation source. Deep level transient spectroscopy (DLTS) was utilized to identify the energy levels of the defects in question and thereby information about their origin. The spectra of the PL and DLTS results were compared to give the best possible identification, taking into account the literature data.

The results revealed interesting trends for defects that might prove to be single-photon emitters in the future in addition to the previously observed G-centers. Some of the best candidates in the telecom range found in our experiments are the W- and X-lines. The W- and X-lines are believed to originate from competing differently sized complex clusters of interstitial silicon. By comparing the PL and DLTS spectra, a possible structure for the X-line has been proposed and discussed.

Acknowledgements

First of all, I would like to thank the University of Oslo for giving me the opportunity to learn and grow over these past few years. I also need to express my gratitude to my supervisor Andrej Kuznetsov, co-supervisors David Rivas Gongora and Robert Karsthof for their immense help during these last stressful months, this could not have been done without you. The PL samples could not have been analysed without the help of the brilliant PL minds of Augustinas Gelackas and David Gongora. Robert Karstofhs help with DLTS setup and analysis were invaluable to this assignment. For my lab work, Viktor Bobal and Halvor Dolva was always there to help. Thank you all for getting me through this. The Research Council of Norway is acknowledged for the support to the Norwegian Micro- and Nano-Fabrication Facility, NorFab, project number 295864.

Contents

I Introduction 2

1 Introduction 3
- 1.1 Problem statement . . . 3
- 1.2 Research method . . . 3
- 1.3 Limitations . . . 3
- 1.4 Thesis outline . . . 3

II Background 5

2 An Update of Solid State Physics 6
- 2.1 Periodicity and Lattices . . . 6
- 2.2 Reciprocal Lattice . . . 6
- 2.3 Brillouin Zone . . . 7
- 2.4 Electrons in Periodic Structures . . . 7
  - 2.4.1 Electronic Energy Bands . . . 8
  - 2.4.2 Nearly Free Electron Model . . . 8
  - 2.4.3 Tight Binding Model . . . 8
- 2.5 Effective Mass . . . 9
- 2.6 Density of States . . . 9
- 2.7 Phonons . . . 10

3 Physics of Semiconductors 11
- 3.1 Semiconductors . . . 11
- 3.2 Electrons and Holes in Semiconductors . . . 12
  - 3.2.1 The Fermi Level . . . 12
  - 3.2.2 Effects of Doping . . . 13
  - 3.2.3 Extrinsic Carrier Concentration . . . 13
  - 3.2.4 Excess Carriers . . . 14
  - 3.2.5 Direct Recombination . . . 15
  - 3.2.6 Indirect Recombination . . . 15
  - 3.2.7 Mobility . . . 16
  - 3.2.8 Transport Equations . . . 16
- 3.3 pn-junction . . . 17
  - 3.3.1 Contact Potential . . . 17
  - 3.3.2 Depletion Region . . . 19
- 3.4 Metal-Semiconductor Junction . . . 20
  - 3.4.1 Schottky Barrier . . . 20

3.4.2 Rectifying and Ohmic Contacts 21
3.4.3 The Depletion Region and its Capacitance 21
3.5 Excitons 22

4 Point Defects in Semiconductors **23**
4.1 Point Defects 23
4.2 Doping 23
4.3 Secondary Defects 24
4.4 Impurities and Secondary Defects 24

5 Photoluminescence **25**
5.1 Luminescence 25
5.2 Photoluminescence 25
5.2.1 Fluorescence 26
5.2.2 Phosphorescence 26
5.3 Radiative Recombination Processes 27
5.4 Capture and Emission Processes 27
5.5 Non-Radiative Recombination Processes 28
5.5.1 Auger Recombination 28
5.5.2 Shockley Reed Hall Recombination 28
5.5.3 Surface Recombination 29

6 Single-Photon Emitters in Silicon **30**
6.1 Single-Photon Sources 30
6.2 Second Order Coherence, $g^{(2)}$ 31
6.3 State Vector 31
6.4 Photon Number Probabilities 32
6.5 Indistinguishability and Purity 32
6.6 Single-Photon Emitters in Silicon 33

7 Material Properties of Silicon **34**
7.1 Growth 34
7.2 Crystal Structure 35
7.3 Impurities and Defects 35
7.3.1 Oxygen 35
7.3.2 Carbon 37
7.3.3 Nitrogen 37
7.3.4 Metal Impurities 37
7.3.5 Vacancies 39
7.4 G-line 39
7.5 W-line and X-line 39
7.6 C-line and P-line 39

8 Quantum Technology **40**
8.1 Important Principles of Quantum Physics 40
8.1.1 Heisenberg Uncertainty Principle 40
8.1.2 Superposition 40
8.1.3 Entanglement 41
8.1.4 Coherence and Decoherence 41
8.2 Quantum Sensing 41

8.3 Quantum Communications 41
8.4 Quantum Computing 41
8.4.1 Qubit 42
8.4.2 Requirements for Quantum Computing 42
8.4.3 Optical Quantum Computing 43

III Methodology 45

9 Proton Irradiation 46
9.1 Sample Preparation 46
9.2 Proton Irradiation 46

10 Optical Characterization 48
10.1 Photoluminescence Spectroscopy 48

11 Electrical Characterization 50
11.1 Capacitance measurements 50
11.2 DLTS 50
11.2.1 Principles of Operation 50
11.2.2 Method 52

12 Four-Point Probe Measurement 53

IV Results 54

13 Simulation of Ion Impacts 55

14 Photoluminescence Spectroscopy 57

15 Four Point Measurement 62

16 Electrical Characterization 63
16.1 CV measurements 63
16.2 DLTS 64

V Conclusion and Future Work 71

17 Conclusion 72

18 Future Work 73

A Photon Statistics I - Quantized Electric field and Operator Notion 74

B Photon Statistics II - Second-Order Coherence, $g^{(2)}$ 76

C PL spectra 77

D CV measurements 79

E Rate Windows **81**

List of Figures

2.1 Brillouin zone 7
2.2 Tight binding model 8
2.3 Optical and acoustic phonons 10

3.1 Band gap semiconductor and insulator 11
3.2 Electron-phonon interaction 12
3.3 Current direction vs particle direction 17
3.4 pn-junction and potentials 18
3.5 Band bending in pn-juntctions 18
3.6 Depletion region and corresponding electric field 19
3.7 Metal-semiconductor contact 20
3.8 I-V curve Schottky diode 21

5.1 Jablonski diagram of fluorescence and phosphorescence 26
5.2 Radiative recombination processes 27
5.3 Capture and emission processes 28
5.4 Auger recombination 29

6.1 Illustration of antibunching 30
6.2 Hanbury Brown-Twiss interferometer 31
6.3 PL spectra of SD1-SD6 33

7.1 Silicon crystal structure 35
7.2 Thermal donor illustration 37
7.3 Illustration of the G-center 39

8.1 Illustration of superposition 40
8.2 Illustration of entanglement 41
8.3 Qubit illustration 42
8.4 Polarization of photons 43
8.5 Bloch sphere 43
8.6 Illustration of gate operation 44

9.1 Illustration of ion irradiation 47

10.1 PL setup 48
10.2 Laser absorption depth 49

11.1 Illustration of DLTS spectrum 52

12.1 Four-Point Measurement Setup 53

13.1 Depth profile of vacancy distribution 55
13.2 Ion penetration depth 56

14.1 n-type PL spectra 57
14.2 Integrated PL, P-line, W-line and C-line 58
14.3 p-type PL spectra 59
14.4 n and p-type PL spectra 60
14.5 Peak 1, 3a, 3b and 4 61

16.1 $1/C^2$-V for n- and p-type Si 63
16.2 Carrier concentration n-and p-type 64
16.3 DLTS spectrum n-type 65
16.4 DLTS spectrum p-type 66
16.5 Simulated DLTS spectrum n-type 5E12 67
16.6 Simulated DLTS spectrum p-type 5E12 68
16.7 C-T measurements n- and p-type 69
16.8 Comparison PL and DLTS n-type 69
16.9 Comparison PL and DLTS p-type 70

C.1 n-type PL spectra 77
C.2 p-type PL spectra 78
C.3 PL spectra with SD1-SD4 78

D.1 CV measurements n-type 79
D.2 CV measurements p-type 80

E.1 Rate windows for n-type 5E12 sample 81
E.2 Rate windows for p-type 5E12 sample 82

List of Tables

7.1 Energy levels of impurities in silicon 36

9.1 Laser parameters 46
9.2 Fluence details 47

13.1 Vacancy concentration 56

14.1 Parameters of PL peaks 61

15.1 Resistivity of samples 62

16.1 DLTS parameters 68

Part I

Introduction

Chapter 1

Introduction

1.1 Problem statement

There are over a hundred independent optical transitions known in crystalline silicon [14]. Recent research in the near-infrared range have shown independent single-photon emitters related to specific defects [17]. Out of the seven single-photon sources found, one was identified as the G center. The goal of this thesis is to identify the defects that corresponds to the other single-photon sources in the near-infrared range in silicon.

1.2 Research method

My supervisor Andrej Kuznetsov theorized that we could recreate some of the single-photon emitters they found [17] by means of proton irradiation to create defects. Wafers of n- and p-type CZ silicon were cut into 5 samples each and four of each were then irradiated at different fluences while one was kept untouched for reference. We used photoluminescence spectroscopy to compare the spectra from my samples to the spectra of the single-photon emitters Durand et al. found [17]. Then we did a four-point measurement to determine resistivity and charge carrier concentration. Lastly deposition of metal contacts were done to measure electronic levels using deep level transient spectroscopy.

1.3 Limitations

There will always be problems with reproducability. The paper this thesis is built on implanted both carbon and protons into silicon when they observed the single-photon sources [17]. In my experiment we only irradiated with protons as we believed this would not alter the result considerable.

1.4 Thesis outline

This thesis is divided into 5 parts; Introduction, Background, Methodology, Results and Conclusion. The Background part gives insight into the physics behind semiconductors, some principles needed to understand the equipment used in

Methodology and a brief introduction to applications in quantum technology. In Methodology the different experiments done on the samples are explained and how they operate. The product of the experiments are given in Results and are later compared to literature and discussed. The last part is the Conclusion where the findings are summarized and future work discussed.

Part II

Background

Chapter 2

An Update of Solid State Physics

Part II of this thesis is based on the textbooks of Streetman and Banerjee [39], Kittel [23], Nordby [29] and Tilley [40].

2.1 Periodicity and Lattices

An ideal crystal is constructed by the infinite repetition of identical groups of atoms placed on points called the basis. The set of mathematical points to which the basis is attached is called the lattice and the two gives the crystal structure. In three dimensions there are 14 lattices called the Bravais lattices and these are made by adding one of the seven lattice systems with one of the three centerings. The different centerings are primitive (P) with lattice point on the corners only; body centered (I) with one extra lattice point at the center, or face centered (F) with one additional lattice point at the faces of the cell.

2.2 Reciprocal Lattice

The reciprocal lattice is an inverted structure of the crystal lattice with its own lattice vectors created from the primitive lattice vectors $\mathbf{a}_1$, $\mathbf{a}_2$ and $\mathbf{a}_3$. These vectors are

$$\mathbf{b}_1 = 2\pi \frac{\mathbf{a}_2 \times \mathbf{a}_3}{\mathbf{a}_1 \cdot \mathbf{a}_2 \times \mathbf{a}_3} \tag{2.1}$$

$$\mathbf{b}_2 = 2\pi \frac{\mathbf{a}_3 \times \mathbf{a}_1}{\mathbf{a}_1 \cdot \mathbf{a}_2 \times \mathbf{a}_3} \tag{2.2}$$

$$\mathbf{b}_3 = 2\pi \frac{\mathbf{a}_1 \times \mathbf{a}_2}{\mathbf{a}_1 \cdot \mathbf{a}_2 \times \mathbf{a}_3} \tag{2.3}$$

The brilliance of the reciprocal lattice is the ability to analyse interactions in reciprocal space (often called k-space or momentum space) where the electrons are mathematically handled. By using these reciprocal vectors one can map points in the reciprocal lattice

$$\mathbf{G} = v_1\mathbf{b}_1 + v_2\mathbf{b}_2 + v_3\mathbf{b}_3 \tag{2.4}$$

where v_1, v_2 and v_3 are integers and $\mathbf{G}$ is a reciprocal lattice vector.

2.3 Brillouin Zone

The information of the crystal structure of a perfect solid is found from the unit cell which goes in repetition all through the material. Electrons are delocalized quantum mechanical particles and their energy levels are not functions of positions in real space but exist as quantized and distinct levels in k-space. The Brillouin zone is a Wigner-Seitz cell of the reciprocal lattice and information from the 1. Brillouin zone repeats itself in the others and this is often just referred to as the Brillouin zone. This can be constructed by drawing lines from the reciprocal point in question to the nearest neighbors and then draw perpendicular lines halfway across these lines as seen in figure 2.1 The informa-

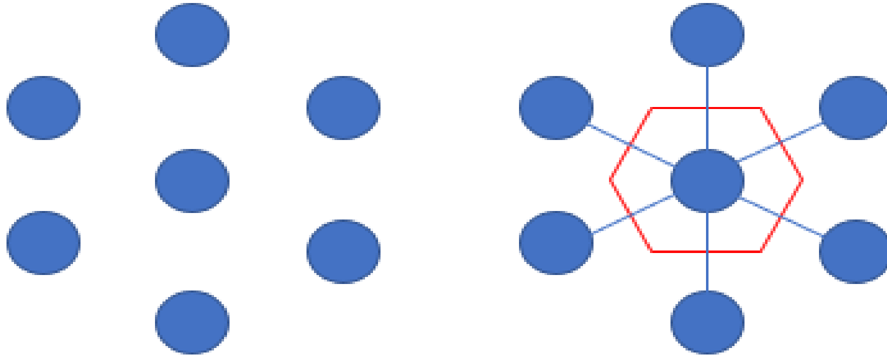

Figure 2.1: Left side show reciprocal lattice points and right is the Brillouin zone marked in red from these points

tion from solving the Schrödinger equation for different points in the Brillouin zone will give eigenvalues and eigenvectors. Since momentum and position are conjugated variables, optical transitions and electron distribution in real space can be extracted from this.

2.4 Electrons in Periodic Structures

Particles such as electrons in quantum systems do not obey classical Newtonian mechanics. To explain the behavior of the electron wave function in such systems the Schrödinger equation can be used

$$-\frac{\hbar}{2m}\bigtriangledown^2\psi(\mathbf{r}) + V\psi(\mathbf{r}) = E\psi(\mathbf{r}) \tag{2.5}$$

Equation 2.5 is the time-independent Schrödinger equation where $\bigtriangledown$ is the Laplacian operator, ψ is the wave function, V is the potential and E is the energy of the system. To solve the Schrödinger equation for electrons in a periodic potential, Bloch's theorem states that the solution must come in the form of a plane wave modulated by a periodic function

$$\psi(\mathbf{r}) = e^{i\mathbf{k}\cdot\mathbf{r}}u(\mathbf{r}) \tag{2.6}$$

where **r** is the position, **k** is the wave vector and u is the periodic potential.

2.4.1 Electronic Energy Bands

In solids, electronic energy bands are energy intervals that possesses electronic states in which the electrons can occupy. The problem to find the eigenvalues and eigenvectors is usually done by Fourier transformation of the Schrödinger equation (differential equation) into an algebraic equation. An exact solution can be found for only a few cases and for the rest some approximations must be used.

2.4.2 Nearly Free Electron Model

In the nearly free electron model the electrons are treated as a free electron gas with the use of perturbation theory for the periodic potential of the crystal. Electronic waves get scattered from the crystal potential and the bands emerge from interference from the waves which gives standing waves at the Brillouin zone edges.

2.4.3 Tight Binding Model

This model has its basis in the energy levels of a single atom. The Pauli principle states that identical electrons can not occupy the same level and when two identical atoms are brought together a splitting in the energy level occurs to satisfy this principle as seen in figure 2.2 For a bulk sample the splitting occurs

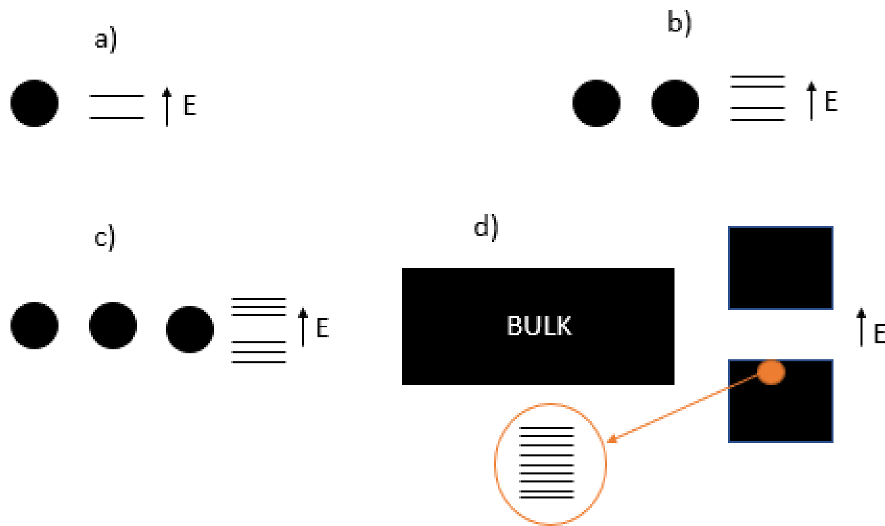

Figure 2.2: a) Two energy levels of an atom. b) and c) Splitting in the energy levels. d) A bulk sample where the level are indistinguishable

numerous times and the levels become so closely spaced they behave as a continuum of allowed states. The region between these energy bands are called the band gap, E_G, and in this interval there are no allowed states for electrons to occupy.

2.5 Effective Mass

In a crystal, electron behavior is not the same as in free space because they interact with the periodic potential of the lattice. This interaction must be taken into account when doing electrodynamic calculations. The electron momentum is given by p = mv = $\hbar\mathbf{k}$ and the kinetic energy is

$$E = \frac{1}{2}mv^2 = \frac{1}{2}\frac{p^2}{m} = \frac{\hbar^2}{2m}\mathbf{k}^2 \tag{2.7}$$

By taken the second derivative with respect to the wavevector $\mathbf{k}$ one finds that the electron mass is inversely related to the band curvature

$$\frac{d^2E}{d\mathbf{k}^2} = \frac{\hbar^2}{m} \tag{2.8}$$

By sorting one finds the effective mass to be

$$\boxed{m^* = \frac{\hbar^2}{\frac{d^2E}{d\mathbf{k}^2}}} \tag{2.9}$$

and this equation (2.9) relates the mass to the periodic potential of the crystal through its band structure.

2.6 Density of States

The density of states (DOS) describes the number of states that can be occupied per energy and per volume in a material. The material can be modeled as a cube with sides L who possess N^3 primitive cells. By applying the boundary conditions that the wavefunction is zero at the edges, k is determined by the condition

$$exp[i(k_x x + k_y y + k_z z)] \equiv exp[i(k_x(x+L) + k_y(y+L) + k_z(z+L))] \tag{2.10}$$

This gives the allowed values for the different dimensions of k

$$k_{x,y,z} = 0, \pm\frac{2\pi}{L}, \pm\frac{4\pi}{L}, ..., \frac{N\pi}{L} \tag{2.11}$$

which means that there in one allowed value of $\mathbf{k}$ per volume $(2\pi/L)^3$. The total number of states with wavevector less than k in a sphere with radius k is

$$N = 2 \cdot \left(\frac{4\pi k^3}{3}\right)\left(\frac{L}{2\pi}\right)^3 = \frac{V}{3\pi^2}k^3 \tag{2.12}$$

where the extra two is from the spin of electrons. From the dispersion relation we have

$$E = \frac{\hbar^2 k^2}{2m} \tag{2.13}$$

which gives

$$k = \sqrt{\frac{2mE}{\hbar^2}} \tag{2.14}$$

By substituting eq.2.12 with eq.2.14, the density of states per energy can be found

$$N(E) = \frac{dN}{dE} = \frac{V}{2\pi^2}\left(\frac{2m}{\hbar^2}\right)^{\frac{3}{2}} E^{\frac{1}{2}} \tag{2.15}$$

2.7 Phonons

Atoms in the lattice atoms will vibrate around an equilibrium position even at extremely low temperatures. A phonon is a quantum of energy for these quantized modes of vibrations. The energy of these elastic modes take the form of an harmonic oscillator with

$$E = \left(n + \frac{1}{2}\right)\hbar\Omega \tag{2.16}$$

where n is the quantum number or phonons in one mode and Ω the angular frequency which gives the zero point energy $\frac{1}{2}\hbar\Omega$. In one dimension with only one atomic type, the angular frequency is given by

$$\Omega(k) = 2\sqrt{\frac{K}{M}}\sin\frac{ka}{2} \tag{2.17}$$

where K is the force constant, M is the mass of the atom and a is length of the cell. The angular frequency is periodic and all vibrations are then given between $-\frac{\pi}{2} < k \leq \frac{\pi}{2}$. There are acoustical- and optical modes of vibrations as seen in figure 2.3. The most important for this paper is the optical phonons

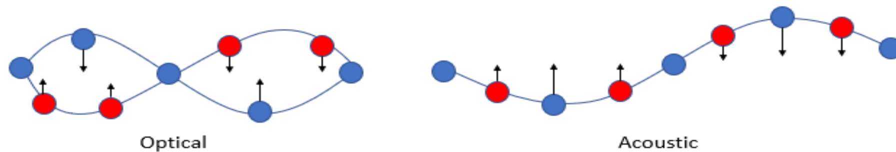

Figure 2.3: Illustration of acoustic and optical phonon

where neighbouring atoms oscillate out of phase. Incoming electromagnetic waves can induce these optical phonons because of the electric field created by the oscillating dipoles (thereby the name optical). The phonons in a material have momentum $\hbar\vec{k}$ and can interact with photons, electrons or nuclei which is important for indirect semiconductors like silicon.

Chapter 3

Physics of Semiconductors

3.1 Semiconductors

Semiconductors are materials with an electrical conductivity that is in between that of a metal and an insulator. This conductivity can be altered by temperature changes, optical excitation and by impurities or dopants. Silicon is an elemental semiconductor, which means they consist of only one type of atoms. A semiconductor at 0 K acts as an insulator because the states in the valence band is filled and there is no possible available states for the electrons to move into without the aid of external energy. The difference between insulators and semiconductors lies in the size of the band gap. The smaller band gap in semiconductors allow for a reasonable amount of excitations from the valence to the conduction band as a result of thermal or optical energy greater than the band gap as seen in figure 3.1. There are indirect and direct semiconductors and for

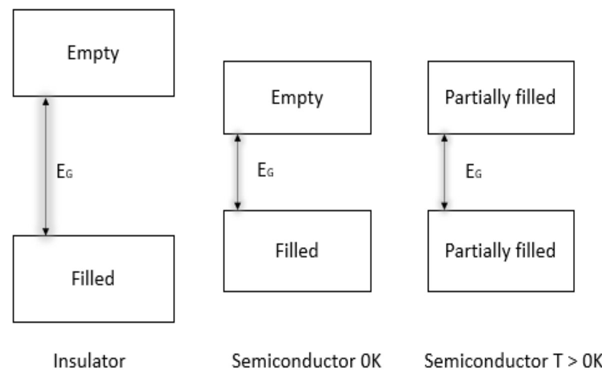

Figure 3.1: Band gap for insulator, semiconductor at 0K and semiconductor at T > 0K

direct semiconductors, the valence band maximum and conduction band minimum have the same position in **k**-space. In indirect the positions are different and electrons must undergo a change in momentum to transverse between the two and this is done by electron-phonon interactions as seen in figure 3.2 So the

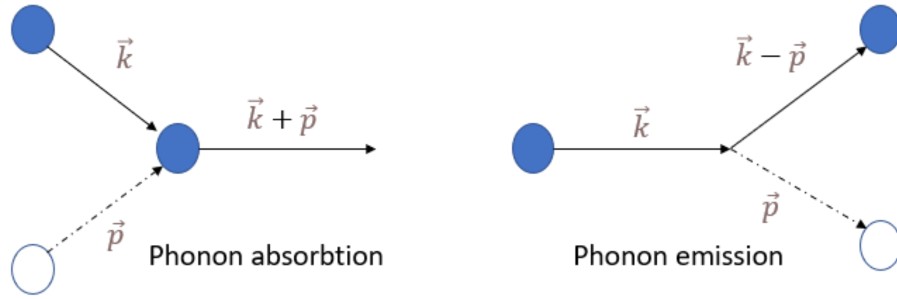

Figure 3.2: Illustration of phonon-electron interaction

energy conserved in an indirect band gap material will be

$$\hbar\omega = E_f - E_i \pm \hbar\Omega \tag{3.1}$$

where the $\pm$ corresponds to emission and absorption and $\hbar\Omega$ is the energy of the photon. An intrinsic semiconductor is a perfect crystal without defects and are worth mentioning. These do not exist in practice but purification of materials such as silicon can get the impurities down to the parts per billion (ppb) range.

3.2 Electrons and Holes in Semiconductors

At 0K, an intrinsic semiconductor has a filled valence band and an empty conduction band. When the temperature is increased, some electrons are excited to the conduction band by the thermal energy. This leaves some empty states in the valence band and this absence of electrons are called holes. The electrons in the conduction band have many available states and are free to move through the material via these unoccupied states. By keeping track of the holes in the valence band and the electrons in the conduction band, one can ascertain the charge transport and current in the semiconductor.

3.2.1 The Fermi Level

The Fermi level is a mathematical construct to describe the concentration of charge carriers in the material. Electrons in solids obey Fermi-Dirac statistics and the distribution of electrons at different energy levels is given by the Fermi-Dirac distribution function

$$\boxed{f(E) = \frac{1}{1 + e^{(E-E_F)/k_B T}}} \tag{3.2}$$

where k_B is Boltzmann's constant, T is the temperature, E is the energy level in question and E_F is the Fermi level. The distribution function gives the probability of finding an electron at an energy level for a certain temperature. In applying this distribution function to semiconductors it is important to note that it is the probability of occupancy of an available state with energy E. If this state is in the band gap of an intrinsic semiconductor, it is not possible to find an electron here since these energy states are forbidden. This distribution

function also gives the result that at 0K, all available energy states are filled up to the Fermi level.

3.2.2 Effects of Doping

By doping a semiconductor, one can alter the equilibrium carrier concentrations to be different from the intrinsic carrier concentration, n_i. If the excess carrier are electrons, the semiconductor is called n-type and if it is holes it is called p-type. In silicon this can be done by doping with atoms of column III (p-type) or column V (n-type) and the newly introduced atoms substitute the host atoms. Atoms of column III have one less valence electron and column V have one extra valence electron in the in respect to silicon. These dopants introduce additional levels in the band gap near the valence (p-type) and conduction band (n-type). In a n-type at 0K, this level is filled with electrons and only a small amount of thermal energy is required to excite them to the conduction band. When the temperature is raised, this level "donates" its electrons to the conduction band and is called a donor level. In p-type the level near the valence band is empty of electrons at 0K and with a little thermal energy electrons from the valence band gets excited to this level. This level is called an acceptor level since it "accepts" electrons from the valence band at small thermal energies.

3.2.3 Extrinsic Carrier Concentration

The concentration of carriers in extrinsic semiconductors can be calculated using the Fermi distribution and the density of states. Concentration of electrons in conduction band and holes in valence band

$$n_0 = \int_{E_C}^{\infty} f(E)N(E)dE \tag{3.3}$$

$$p_0 = \int_{0}^{E_V} f(E)N(E)dE \tag{3.4}$$

Where f(E) is the Fermi distribution function, N(E)dE is the density of states in range dE and the 0 subscript means under equilibrium conditions. By doing the integration for electrons in the conduction band

$$n_0 = \int_0^{\infty} N(E)f(E)dE = \frac{1}{2\pi^2}\left(\frac{2m}{\hbar^2}\right)^{\frac{3}{2}} e^{E_F/kt} \int_0^{\infty} E^{\frac{1}{2}} e^{-E/kT} \tag{3.5}$$

where 0 is taken as E_C and the assumption the Fermi distribution function take the form f(E) = $e^{(E_F - E)/kT}$. The integral on the right hand side of Eq. 3.5 is of the form

$$\int_0^{\infty} x^{\frac{1}{2}} e^{-ax} = \frac{\sqrt{\pi}}{2a\sqrt{a}} \tag{3.6}$$

This gives

$$n_0 = 2\left(\frac{2\pi m_n^* kT}{h^2}\right)^{\frac{3}{2}} e^{(E_F - E_C)/kT} \tag{3.7}$$

Where the potential of the lattice is related through the effective mass m_n^*. We can represent the integration by the effective density of states, N_C and N_V

located at the conduction band and valence band edge, respectively. This gives the concentration of electrons in the conduction band and holes in the valence band to be

$$n_0 = N_C e^{(E_F - E_C)/k_B T} \tag{3.8}$$

$$p_0 = N_V e^{(E_C - E_V)/k_B T} \tag{3.9}$$

Provided thermal equilibrium, these equations are valid for extrinsic and intrinsic materials. The product of n_0 and p_0 is constant given material and temperature, even though the doping is varied.

$$n_0 p_0 = N_c N_V e^{-E_G/k_B T} \tag{3.10}$$

This is the same as the product of the intrinsic carrier concentrations, n_i and p_i, and gives a important relation

$$n_0 p_0 = n_i^2 \tag{3.11}$$

This relations gives an easier way to obtain the carrier concentrations

$$n_0 = n_i e^{(E_F - E_i)/kT} \tag{3.12}$$

$$p_0 = n_i e^{(E_i - E_F)/kT} \tag{3.13}$$

where E_i is the intrinsic level the Fermi level would take in a intrinsic material.

3.2.4 Excess Carriers

There are different methods to create an excess of carriers in semiconductor materials. One way to create an excess of carriers as opposed to the thermal equilibrium value is by optical excitation. Electrons and holes created by this process must eventually recombine, but while they remain in their excited state they may contribute to the conductivity of the material. Photons need energy

$$hv \geq E_G \tag{3.14}$$

to excite electrons from the valence band into the conduction band. The total carrier concentration can be found by using the quasi-Fermi levels F_n and F_p

$$\boxed{n = n_i e(F_n - E_i)/kT} \tag{3.15}$$

$$\boxed{p = n_i e(E_i - F_p)/kT} \tag{3.16}$$

The excess carriers induced creates a deviation from the equilibrium values and the quasi-Fermi levels describes how far the carrier concentrations are from their equilibrium values n_0 and p_0.

3.2.5 Direct Recombination

Direct recombination is a spontaneous event, meaning the probability is constant through time. The excess concentration of carriers decays by electrons in the conduction band recombining with holes in the valence band and the energy lost by this process is given up as photons. Since the probability of recombination is constant in time, the decay in excess carriers will be an exponential. The concentration of electrons in the conduction band changes at a rate

$$\frac{dn(t)}{dt} = \alpha_r n_i^2 - \alpha_r n(t)p(t) \tag{3.17}$$

where α_r is a recombination constant, $\alpha_r n_i^2$ is the thermal generation rate and α_rn(t)p(t) is the recombination rate. The total concentration expressed in terms of n_0 and p_0 and the excess carrier concentrations δn(t) and δp(t) is

$$\frac{d\delta n(t)}{dt} = \alpha_r n_i^2 - \alpha_r [n_0 + \delta n(t)][p_0 + \delta p(t)] \tag{3.18}$$

$$\frac{d\delta n(t)}{dt} = -\alpha_r [(n_0 + p_0)\delta n(t) + \delta n^2(t)] \tag{3.19}$$

given that the initial electron and hole concentrations are equal, and the change in excess carrier concentration Δn(t) = Δp(t) right after t=0. For low level injection and if the material is extrinsic, the δn^2 term and the equilibrium minority carrier concentration can be neglected.

$$\frac{d\delta n(t)}{dt} = -\alpha_r p_0 \delta n(t) \tag{3.20}$$

for a p-type semiconductor ($p_0 >> n_0$). So the excess electron concentration decays

$$\delta n(t) = \Delta n e^{-\alpha_r p_0 t} = \Delta n e^{-t/\tau_n} \tag{3.21}$$

as an exponential from the initial excess carrier concentration Δn with a decay constant τ_n which is often called the minority carrier lifetime. With low injection the carrier lifetime can be written as

$$\tau_n = \frac{1}{\alpha_r (n_0 + p_0)} \tag{3.22}$$

which is valid for both n- and p-type.

3.2.6 Indirect Recombination

In some semiconductor materials the probability of direct recombination is small and they often occur via recombination centers in the band gap, a so called indirect recombination. The recombination centers in the band gap are the result of impurities or lattice defects and the energy lost by recombination are usually given up as heat or a photon. The center must have the ability to receive one type of carrier and capture the opposite type of carrier for recombination to occur. The recombination happens at two steps; hole capture and electron capture. The hole capture is equal to an electron at the recombination level falling to the valence band and leaving behind an empty state, a hole. The

conduction band electron then falls into this empty state and a recombination have occurred. Recombination may be delayed because the thermal energy have a tendency to reexcite the carrier in the first step before the second step happens. This is most common in shallow levels i.e. levels near the bands. If a reexcitation is the most probable event after the initial step, the level is called a trapping level. If capture of the opposite carrier is the most probable, the level is called a recombination center.

3.2.7 Mobility

To calculate current flow in electric or magnetic fields, carrier concentration and their collisions with the lattice and impurities must be considered. These interactions will have an effect on how easy electrons and holes drift through the material, called the mobility. The mobility is dependent on temperature which influence the thermal velocity of the carriers and the thermal motion of the lattice. If both electrons and holes contribute to the current density in an electric field ξ

$$J = q(n\mu_n + p\mu_p)\xi = \sigma\xi \tag{3.23}$$

where σ is the conductivity, μ_n and μ_p is the mobility for electrons and holes, respectively. The mobility can be expressed as

$$\mu_{n/p} = \frac{q\bar{t}}{m^*_{n/p}} \tag{3.24}$$

where $\bar{t}$ is the mean time between scattering events called the mean free time.

3.2.8 Transport Equations

In addition to the current density from drift in electric or magnetic fields, diffusive currents must be taken into account when looking at the total current density in a semiconductor. Electrons and holes diffuse in the direction of decreasing concentration of the two carriers and the particle flux density in x-direction

$$\phi_n = -D_n \frac{dn(x)}{dx} \tag{3.25}$$

$$\phi_p = -D_p \frac{dp(x)}{dx} \tag{3.26}$$

where D_n and D_p is the diffusion coefficient for electrons and holes, respectively. The current density is found by multiplying the particle flux density by the charge

$$J_n(diff) = qD_n \frac{dn(x)}{dx} \tag{3.27}$$

$$J_p(diff) = -qD_p \frac{dp(x)}{dx} \tag{3.28}$$

With an electric field in x-direction we get contributions from both drift and diffusion to the current density

$$J_n(x) = q\mu_n n(x)\xi(x) + qD_n \frac{dn(x)}{dx} \tag{3.29}$$

$$J_p(x) = q\mu_p p(x)\xi(x) - qD_p\frac{dp(x)}{dx} \tag{3.30}$$

and the total current density is the sum

$$\boxed{J(x) = J_n(x) + J_p(x)} \tag{3.31}$$

3.3 pn-junction

3.3.1 Contact Potential

A pn-junction is a composition between a p- and n-type material. When the two are brought together, diffusion of majority carriers from n- to p-side and vice versa occurs because of the large concentration gradients at the two sides. The diffusing carriers leave behind uncompensated donor ions (N_d^+) at the n-side and uncompensated acceptor ions (N_a^-) at the p-side. These uncompensated regions creates an electric field that oppose the diffusion current with a opposite drift component as seen in figure 3.4 The electric field ξ goes from positive to negative

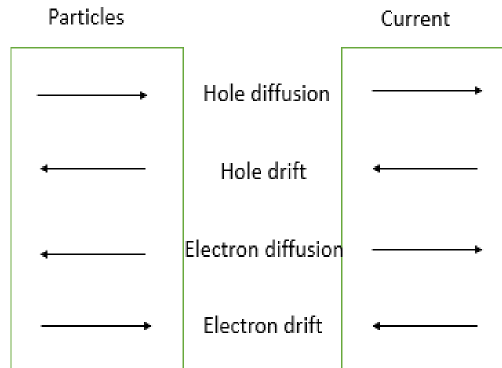

Figure 3.3: Directions of particles and current for a pn-junction with p-side left and n-side right

and equalizes the diffusion current to create a equilibrium where no net current crosses the junction and no net build-up of carriers at the sides

$$J_p(drift) + J_p(diff) = 0 \tag{3.32}$$

$$J_n(drift) + J_n(diff) = 0 \tag{3.33}$$

There is a potential difference V_0 over the transition region where the electric field is. By assuming $\xi = 0$ outside the uncompensated areas, the potential is constant in the p and n region as seen on figure 3.5 In the region between n and p there is a gradient in the potential

$$\xi = -\frac{dV}{dx} \tag{3.34}$$

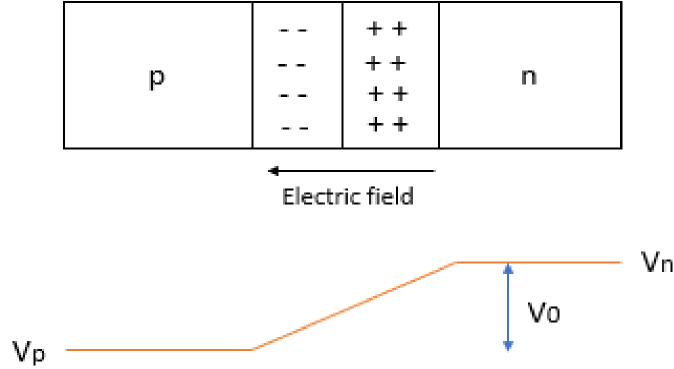

Figure 3.4: Top shows pn-junction with uncompensated areas and direction of electric field. Bottom is the corresponding potentials

V_n-V_p = V_0 is called the contact potential and this is a built-in potential barrier that does not cause any current. When brought together, the Fermi levels of the two materials must align and the conduction and valence band bend as seen in figure 3.6 To relate V_0 to the doping concentration we use Eq.3.32 or 3.33

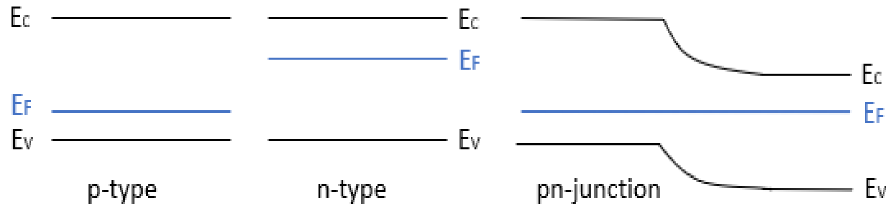

Figure 3.5: Fermi level alignment in pn-junction and resulting band bending

$$J_p(x) = q\left[\mu_p p(x)\xi(x) - D_p\frac{dp(x)}{dx}\right] = 0 \tag{3.35}$$

$$\frac{\mu_p}{D_p}\xi(x) = \frac{1}{p(x)}\frac{dp(x)}{dx} \tag{3.36}$$

by the use of the Einstein relation $\frac{D_p}{\mu_p} = \frac{kT}{q}$

$$-\frac{q}{kT}\int_{V_p}^{V_n} dV = \int_{p_p}^{p_n}\frac{1}{p}dp \tag{3.37}$$

By doing the integration with the fact that V_n-V_p = V_0 and the assumption that the doping concentration is equal to the majority carrier concentrations on each side

$$V_0 = \frac{kT}{q}ln\frac{p_p}{p_n} = \frac{kT}{q}ln\frac{N_a N_d}{n_i^2} \tag{3.38}$$

where the subscript on the hole concentration defines if it is in the n or p region. From these equations it can be shown that the difference in energy for conduction band at p- and n-side is qV_0, same for valence band.

3.3.2 Depletion Region

The region where the electric field appears is called the depletion region W (also called space charge region or transition region). Poisson's equation relates the gradient of the field to the space charge

$$\frac{d\xi(x)}{dx} = \frac{q}{\epsilon}(p - n + N_d - N_a) \tag{3.39}$$

where ϵ is the permittivity of the material. The depletion approximation assumes there is a negligible amount of carriers in the depletion region so n and p can be neglected resulting in a electric field distribution

$$\frac{d\xi}{dx} = \frac{1}{\epsilon}(-qN_a), \quad -x_p < x < 0 \tag{3.40}$$

$$\frac{d\xi}{dx} = \frac{1}{\epsilon}(qN_d), \qquad 0 < x < x_n \tag{3.41}$$

where the boundaries and distributions is seen in figure 3.7 The electric field

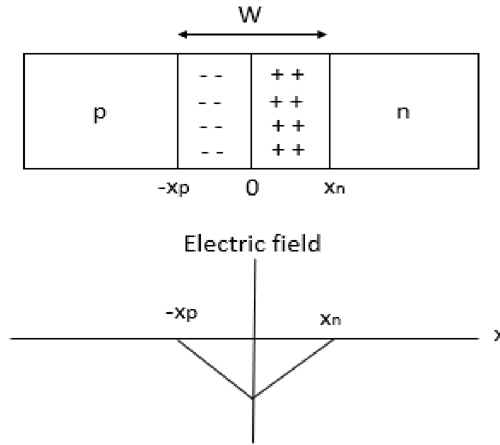

Figure 3.6: Top shows pn-junction with depletion region boundaries. Bottom is the electric field distribution in the depletion region

has its maximum ξ_0 at x = 0 and can be found by integration

$$\int_{\xi_0}^{0} d\xi = \frac{q}{\epsilon}N_d \int_{0}^{x_n} dx, \qquad 0 < x < x_n \tag{3.42}$$

or

$$\int_{0}^{\xi_0} d\xi = -\frac{q}{\epsilon}N_a \int_{-x_p}^{0} dx, \quad -x_p < x < 0 \tag{3.43}$$

which yields

$$\xi_0 = -\frac{q}{\epsilon}N_d x_n = -\frac{q}{\epsilon}N_a x_p \tag{3.44}$$

The width of the depletion region can be found by relating the electric field to the contact potential

$$V_0 = -\int_{x_p}^{x_n} \xi(x)dx \tag{3.45}$$

$$V_0 = -\frac{1}{2}\xi_0 W \tag{3.46}$$

By using the values for ξ_0, the charge balance requirements $x_n N_d = x_p N_a$ and $W = x_n + x_p$

$$V_0 = \frac{1}{2}\frac{q}{\epsilon}\frac{N_a N_d}{N_a + N_d}W^2 \tag{3.47}$$

which gives the width of the depletion region

$$\boxed{W = \left[\frac{2\epsilon V_0}{q}\left(\frac{N_a + N_d}{N_a N_d}\right)\right]^{\frac{1}{2}}} \tag{3.48}$$

3.4 Metal-Semiconductor Junction

3.4.1 Schottky Barrier

This type of junction is widely used for its properties as a rectifier or a ohmic contact. In a metal-semiconductor (n-type) junction, charge transfer will occur upon contact until the Fermi levels have been aligned. We get a depletion region at the interface where uncompensated donor ions in the semiconductor are matched by the negative charge on the metal as seen in figure 3.8 The difference

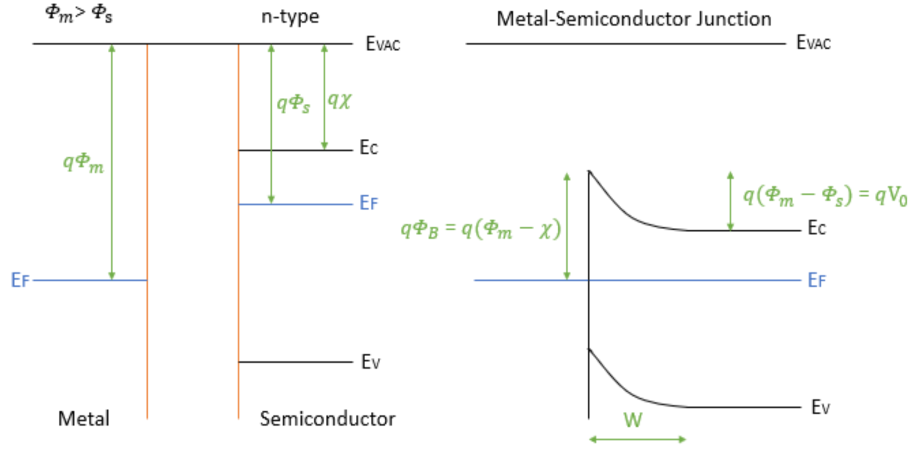

Figure 3.7: Metal and semiconductor before and after contact is made

in work functions (Φ_m and Φ_s) of the materials give the contact potential V_0 which inhibit net current across the depletion region W. The work function is the energy needed to take one electron from the Fermi level to vacuum. The potential barrier Φ_B is the difference in work function of the metal Φ_m and the electron affinity χ, which is the energy needed to get an electron from the conduction band to vacuum. This barrier controls electron injection from the metal into the semiconductor. The contact potential can be reduced or elevated by applying forward or reverse bias voltage which alter the width of the depletion region W. The same logic can be applied to p-type semiconductors which will leave a positive charge on the metal from diffusing holes compensated by

negative charge on the semiconductor from of uncompensated ionised acceptors. The equilibrium contact potential V_0 which will inhabit net current flow across the depletion region will be Φ_s-Φ_m.

3.4.2 Rectifying and Ohmic Contacts

By applying a forward biased voltage V to the Schottky barrier, the contact potential will be reduced from V_0 to V_0-V in an metal-semiconductor junction (n-type). By lowering the barrier, electrons from the conduction band in the semiconductor can now diffuse over into the metal. If the applied bias is reverse, the barrier would increase and electron diffusion would be negligible. The flow of electrons from metal to semiconductor is obstructed by the potential barrier Φ_B. The Schottky barrier diode is rectifying and have easy current flow in one direction from majority carriers, and little current flow in the opposite. The diode equation

$$I = I_0 \left(e^{qV/kT} - 1 \right) \tag{3.49}$$

will yield a I-V curve as illustrated in figure 3.9 In Ohmic contacts the barrier

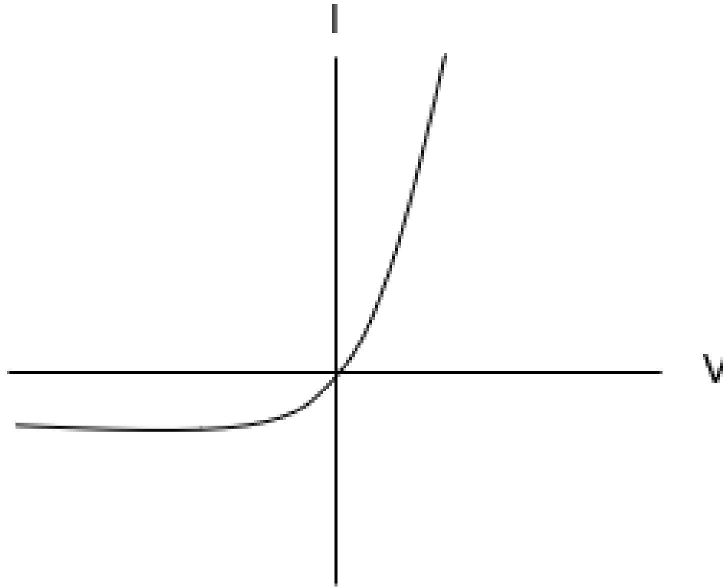

Figure 3.8: I-V curve of a Schottky barrier diode

is low in both directions and current flow is easy both ways. Ohmic contacts follow Ohms law and will have a linear I-V curve.

3.4.3 The Depletion Region and its Capacitance

When a metal and a n-type semiconductor come to contact, carriers will diffuse between the two until the equilibrium contact potential inhibits net current flow

over the depletion region W.

$$W = \left[\frac{2\epsilon(V_0 - V)}{qN_d}\right]^{\frac{1}{2}} \tag{3.50}$$

where ϵ is the dielectric constant of the semiconductor, V_0 is the contact potential or built in voltage, V is the applied voltage, q is the elementary charge and N_d is the doping concentration. The depletion region can be viewed as a parallel plate capacitor with capacitance

$$\boxed{C = \frac{\epsilon A}{W}} \tag{3.51}$$

where A is the contact area. Deep level transient spectroscopy (DLTS) is a method that take advantage of the dependence of the capacitance on the depletion region. DLTS measures the positions of energy levels in the band gap related to specific defects in the semiconductor. This is done by determining the thermal emission rate of electrons and holes trapped at these levels. DLTS also gives information about capture cross sections for electrons and holes, concentration of defects and concentration vs depth profiles. Defects levels near the band edges are called shallow levels and they have an extremely short emission time because their proximity to the band makes them easy to thermally ionize. Deep levels influence the carrier transport because they will act as trapping or recombination centers over large temperature intervals. DLTS requires a rectifying junction for its measurements and this can be obtained by a rectifying metal-semiconductor contact or Schottky contact.

3.5 Excitons

When an electron gets excited it leaves behind a positively charged vacant orbital in the valence band. Since they are of opposite charge, the electrostatic Coulomb force bind them together and this is called a exciton. Frenkel excitions have a small separation while Mott Wannier excitions have a large separation between the electron and hole in real space. It is the Mott Wannier exciton that are interesting in semiconductors and their attraction causes a stabilizing energy which means they have lower energy than an unbound electron and hole. Free excitions are free to move about the lattice and their abundance is dependent on electron and hole concentration. Where it is energetically favorable, excitions may bind to defects or impurities and this can help lower their energy even further. Excitons can bond with donor and acceptor atoms three different ways; neutral acceptor (A^0, X), neutral donor (D^0, X) and ionized donor (A^-, X). This means that three different emission lines may arise from dopants because of bound excitons.

Chapter 4

Point Defects in Semiconductors

This chapter is based on the works of Kittel [23], Nordby [29], Tilley [40], Bathen [8], Streetman [39], Pellegrino [31] and Heinz [22].

4.1 Point Defects

In real life there are no such thing as perfect crystals and the structure will always have defects in the otherwise periodic structure. The simplest localised defect that we can imagine is a mistake at a single atom site and are called point defects. The defects helps to lower the Gibbs free energy of the crystal to the most stable phase

$$G = H - TS \tag{4.1}$$

where H is the enthalpy, T is the temperature and S is the entropy. The entropy can be written as

$$S = k_B lnW \tag{4.2}$$

where W is the number of microstates and k_B is the Boltzmann constant. Both the enthalpy and entropy is dependent on the concentration of defects n_d and we will have an equilibrium point for a certain defect concentration where the free energy is at a minimum.

The most common defect is an empty lattice site where an atom would otherwise be in a perfect crystal and is called a vacancy. Another common point defect is the Frenkel defect where an atom is transported from a lattice site to an interstitial position giving an interstitial and a vacancy.

4.2 Doping

If the defects such as interstital- or substitutional foreign atoms are introduced on purpose, we call it doping and this can drastically alter the properties of the material. Doping can be done in several ways, some of the most common are ion implantation, chemical vapour deposition (CVD) or diffusion processes.

Doping changes the concentration of electrons and holes in a material and in silicon, doping is usually done with boron or phosphor. Phosphorus have one more electron than the silicon atom and when a phosphorus atom take the place of an silicon atom, we will have an extra electron in the lattice

$$Si^x_{Si} \rightarrow P^x_{Si} + e \tag{4.3}$$

If the electron is bound to the position of the phosphorus, it will have a negative effective charge compared to equation 4.3 which is neutral.

4.3 Secondary Defects

There are ways to create intrinsic defects in the material such as irradiation with highly energetic ions of chosen mass. These ions will then collide with lattice atoms and may displace them if their energy is high enough. The collisions between the irradiated ions and the lattice atoms and electrons can be described by S = dE/dR, called the stopping power. This is essentially the energy lost by the ions over a traveled distance. S is divided into two parts, one for the elastic collisions with lattice atoms (S_n) and one for electron interaction (S_e). The core electrons of the lattice atoms act as a screening force and the amount of energy transferred is rarely enough to displace atoms, so S_e can be regarded as a friction force for the incoming ions. S_n can be visualized by elastic collisions so scattering theories can be used. After impact, the defects undergo competing complex reactions and when they reach a steady state the resulting surviving defects are called secondary defects which are thermally stable at room temperature. If a displaced host atom have gained enough energy from collision with the incoming ion, it can in turn displace other atoms and this process is called a collision cascade.

4.4 Impurities and Secondary Defects

There will always be trace amount of other elements than the host element in real crystals. If these are unwanted or not introduced by choice, they are called impurities. A point defect (i.e. impurities, dopants, vacancies or interstitals) in a semiconductor alter the periodic potential of the crystal which introduces additional states for the electrons to occupy. These extra states can have its position in the otherwise forbidden bandgap. Most of the states are optically inactive and act as paths for non-radiative recombination mechanisms, but some are optically active defect centers in which radiative recombination can occur.

Impurities in silicon plays a vital role when it comes to the stability of the secondary defects. The interstitials and vacancies who survive recombination or annihilation at sinks can be stabilized by impurities. The major impurities in silicon are oxygen, carbon, hydrogen and some metals. In n-type and p-type, we will also have dopant impurities and of course the implanted species plays a role. These impurities compete at trapping the migrating defects created by the irradiation and the products depend on the concentration, reactivity and diffusivity of the impurities and migrating defects. The secondary defects which are thermally stable will depend on the concentration as well, but also the temperature at which one composition of defect and impurity is favoured thermally.

Chapter 5

Photoluminescence

This chapter is based on the the books of Che [13], Singh [36] and Nelson [28], and the articles of Pohl [33] and McEwen [24].

5.1 Luminescence

Luminescence is the phenomenon where condensed matter emit photons. This is a radiative process and requires a non-equilibrium carrier concentration in the band or a defect/impurity state to occur. There are different types of luminescence and they are named after the instigator of the non-equilibrium carrier concentration. Excitation of electrons by incoming photons followed by radiative emission is called photoluminescence.

5.2 Photoluminescence

There are different types of photoluminescence which depend on the time it takes between absorption of the incoming photon and emission of a new photon. The fastest process is called fluorescent and the slowest phosphorescent. Figure 5.1 depicts a simplified Jablonski diagram showing some of the internal processes during photoluminescence. An incoming photon of energy $\hbar\omega_1$ excites an electron from ground state (S_0) to an excited state (in figure 4.2 the excited state is S_2) and this process happens almost instantaneously ($\sim 10^{-15}$ s). The wavelength of the photon determines if the electron occupies different vibrational levels (v) of the excited state. The electrons will dissipate energy in various ways on their way back to the stable ground state. Vibrational relaxation is a non-radiative process which dissipates energy through vibrational energy or heat. An electron in a vibrational level of an excited state can cross over to a vibrational level of a lower excited state through a process called internal conversion. This is also a non-radiative process and furthermore, no energy is dissipated during this transition. Both these processes are very fast, $\sim 10^{-12}$-10^{-10} s and $\sim 10^{-14}$-10^{-11} s for vibrational relaxation and internal conversion, respectively. It is possible for an electron to dissipate all the absorbed energy through these non-radiative operations, and this is determined by the probability of radiative and non-radiative recombination events.

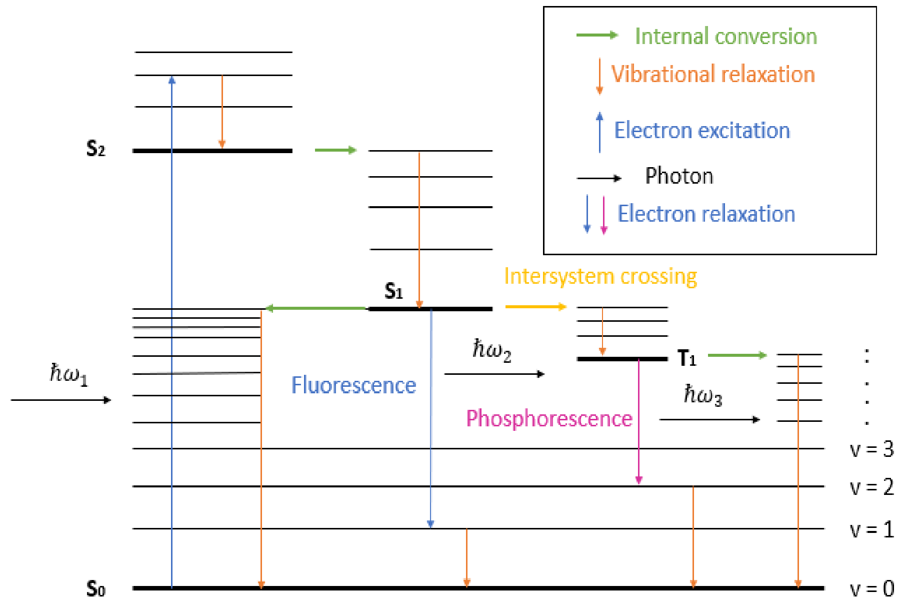

Figure 5.1: Jablonski diagram of fluorescence and phosphorescence

5.2.1 Fluorescence

The radiative emission process in which electrons relax to ground state (S_0) is called fluorescence and is a relatively fast process ($\sim 10^{-9}$-10^{-6} s). The energy dissipated in this process is given up as a photon. This photon will be of lower energy than the initial absorbed photon due to non-radiative dissipation of energy along the way. The material characteristics defines how much energy dissipates due to vibrational relaxation and thereby the difference in incoming and outgoing photon energy and wavelength. This change in incoming and outgoing wavelength is called Stokes shift.

5.2.2 Phosphorescence

From the Pauli principle it is stated that two electrons in the same orbital will always have antiparallel spin in a singlet ground state (S_0). When the electron is excited to a higher state, it retains its spin orientation. Intersystem crossing is when the electron goes from the singlet excited state into a more energetically favourable triplet excited state (T_1) as seen in figure 6.1, thereby flipping its spin orientation. This process is fast (10^{-11}-10^{-6} s) and the resulting relaxation from the triplet excited to singlet ground state inverts the spin again and is called phosphorescence (10^{-3}-100 s). Phosphorescence dissipates more energy in non-radiative processes than fluorescence and the energy of the emitted photon is smaller than the absorbed photon which means phosphorescence has a larger Stokes shift than fluorescence.

5.3 Radiative Recombination Processes

There are several different radiative recombination processes in semiconductors apart from the one shown in figure 5.1. The most important ones are depicted underneath in figure 5.2

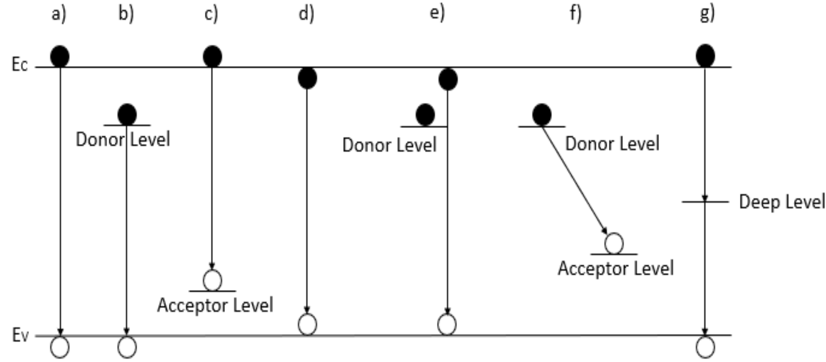

Figure 5.2: Radiative recombination processes in semiconductors

(a) Band-to-band electron and hole recombination

(b) Donor level to valence band transition

(c) Conduction band band to acceptor level transition

(d) Recombination of free exciton

(e) Recombination of bound exciton

(f) Donor and acceptor pair recombination

(g) Deep level defect where both transitions are radiative

5.4 Capture and Emission Processes

The capture and emission processes for electrons and holes at an energy level E_T in the band gap is shown in figure 5.3 where e_n and e_p is the rate of emission for electron and holes to the conduction and valence band, respectively. The rate of capture for an electron from the conduction band or a hole from the valence band are nc_n and pc_p, where c_n and c_p are the capture coefficients. The capture coefficients can be written

$$\boxed{c_n = \sigma_n v_{th_n}} \tag{5.1}$$

$$\boxed{c_p = \sigma_p v_{th_p}} \tag{5.2}$$

where σ_n and σ_p is the capture cross section for electrons and holes, respectively. The thermal velocity of electrons and holes, v_{th_n} and v_{th_p}, is given by

$$v_{th} = \left[\frac{3k_B T}{m^*}\right]^{\frac{1}{2}} \tag{5.3}$$

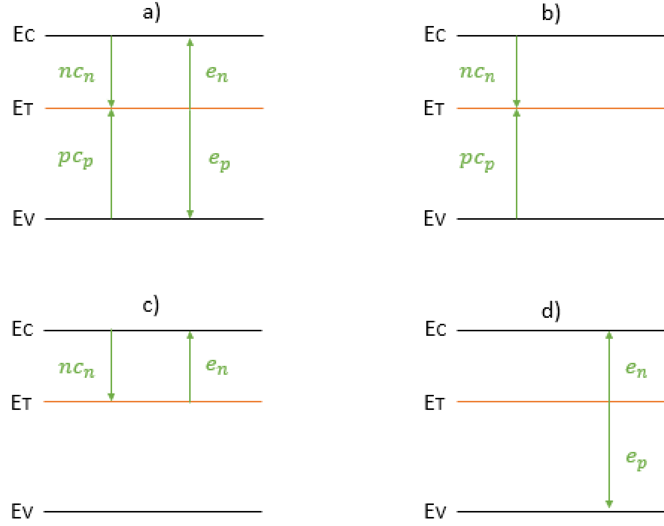

Figure 5.3: a) The total capture and emission processes of this defect level b) Recombination c) Trapping and emission d) Generation

where the effective mass is chosen for either electrons or holes. The rate of emission for electrons is

$$\boxed{e_n(T) = v_{th}\sigma_n N_C e^{-\frac{E_T}{k_B T}}} \tag{5.4}$$

and for holes

$$\boxed{e_p(T) = v_{th}\sigma_p N_V e^{-\frac{E_T}{k_B T}}} \tag{5.5}$$

5.5 Non-Radiative Recombination Processes

5.5.1 Auger Recombination

Auger recombination is non-radiative processes where an electron which recombines with a hole gives up its energy to another electron or hole instead of releasing a photon. The energy absorbed by the electron or hole raise it to a higher state within its band. An illustration of the process is given in figure 5.4

5.5.2 Shockley Reed Hall Recombination

Shockley Reed Hall- or trap assisted recombination and is one of the most dominant recombination processes in silicon. Defects and impurities create additional energy levels in the band gap and these can act as traps for electrons and holes. The energy given up when a electron or hole is trapped is given up as a phonon and they can be released by thermal energy. An illustration for electron trapping and re-excitation is given in figure 5.3 c).

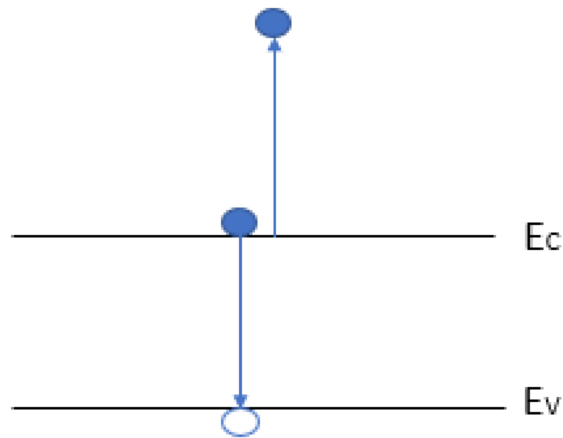

Figure 5.4: Auger recombination where blue and transparent dot indicate electron and hole

5.5.3 Surface Recombination

Defects and dangling bonds are more likely to appear on surfaces of materials such as silicon. Non-radiative recombination can occur at the energy levels caused by these and for especially solar cell application, passivation of the surface is needed.

Chapter 6

Single-Photon Emitters in Silicon

This chapter is based on the works of Aspect [6], Aharonovich [2], Stevens [38] and Bienfang [10].

6.1 Single-Photon Sources

An ideal single-photon source emits exactly one photon at a time. These emitters exhibit antibunching, which means that the time between two succeeding photons is never less than some value τ_c as seen in figure 6.1. There are several

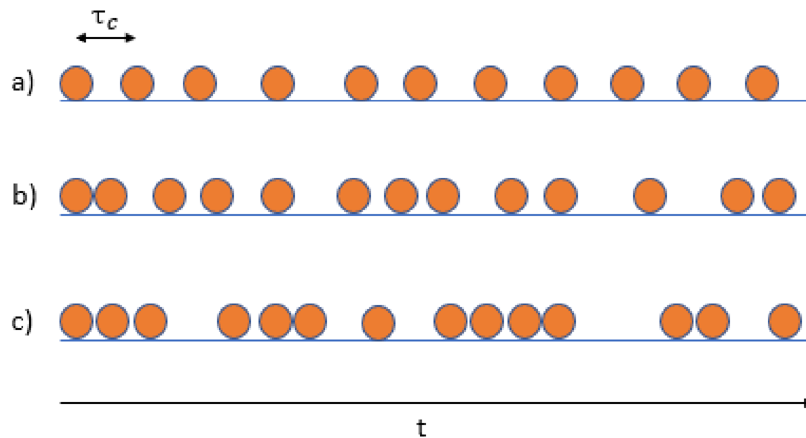

Figure 6.1: Photon emission as a function of time a) antibunching b) random (coherent light) c) bunching (chaotic light)

types of single-photon sources but this paper will focus on the fluorescence of optically active point defects in silicon. This can be viewed as a discrete quantum system and the de-excitation process will yield a single photon which will be indistinguishable from the next photon when the process is repeated.

6.2 Second Order Coherence, $g^{(2)}$

The second order coherence or second order correlation function, $g^2(\tau)$, is the most common method to measure single-photon source quality. $g^{(2)}$ can be measured accurately and is therefore a better measure than the photon number distribution P(n) which can be difficult to ascertain. A Hanbury Brown-Twiss interferometer is usually used to determine $g^{(2)}(\tau)$ and is illustrated in figure 6.2 The incoming optical field in 1 are split at the beamsplitter into 3 and 4

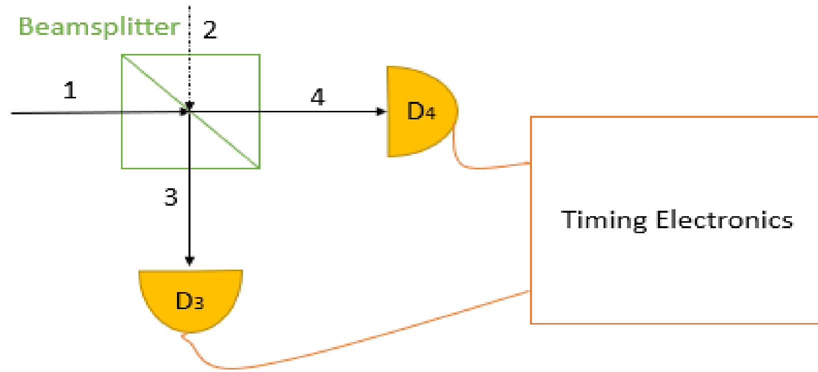

Figure 6.2: Hanbury Brown-Twiss interferometer

and these are incident on two detectors D_3 and D_4, while 2 is the vacuum field. The timing electronics measure the time delay between incident on the different detectors and give a measure of the second order coherence. A common form of $g^{(2)}$ is

$$g^{(2)}(\tau) = \frac{\langle \hat{a}^\dagger(t)\hat{a}^\dagger(t+\tau)\hat{a}(t)\hat{a}(t+\tau)\rangle}{\langle \hat{a}^\dagger(t)\hat{a}(t)\rangle^2} \tag{6.1}$$

where $\hat{a}^\dagger$ is the creation operator and $\hat{a}$ is the annihilation operator which are derived and explained in Appendix A and Appendix B. When $\tau = 0$ we get

$$g^{(2)}(0) = \frac{\langle \hat{n}(t)(\hat{n}(t)-1)\rangle}{\langle \hat{n}(t)\rangle^2} \tag{6.2}$$

where $\hat{n}$ is the number operator explained in Appendix A. For an ideal single photon source, the incoming photon in the Hanbury Brown-Twiss interferometer will have no possibility to be measured at both detectors and $g^{(2)}(0) = 0$. The threshold limit for a single photon emitter is $g^{(2)}(0) < 0.5$.

6.3 State Vector

The state vector describes light emitted from a source into a pure state. The state vector for a quantized electric field can be written in a multi-mode version at position $\vec{r}$ and time t

$$|\Psi(\vec{r},t)\rangle = \sum_{n_1,n_2,n_3,..} c_{n_1}c_{n_2}c_{n_2}..(\vec{r},t)|n_1\rangle|n_2\rangle|n_3\rangle... \tag{6.3}$$

where $c_{n_1,n_2,n_3}...(\vec{r},t)$ is the complex coefficients representing photons in the different modes. If it does not depend on time or space, or these dependencies are baked into the mode

$$|\Psi\rangle = \sum_{n=0}^{\infty} c_n |n\rangle \tag{6.4}$$

An ideal single photon emitter will emit light in the state

$$|\Psi\rangle = |1\rangle \tag{6.5}$$

which contains one photon in one optical mode.

6.4 Photon Number Probabilities

The density matrix gives a quantum representation of both pure and mixed states as opposed to the state vector. The density matrix operator is an ensemble average of pure states

$$\hat{\rho} = \sum_i p_i |\Psi_i\rangle\langle\Psi_i| \tag{6.6}$$

where p_i is the probability that a photon occupies state $|\Psi_i\rangle$. In a pure state, only one of the p_i will be non-zero and this is equal to one. The photon number states can be used as basis and the diagonal elements of the density matrix will contain photon number probabilities

$$P(n) = \langle n|\hat{\rho}|n\rangle \tag{6.7}$$

where P(n) is the probability a source emits n photons and

$$\sum_{n=0}^{\infty} P(n) = 1 \tag{6.8}$$

An ideal single-photon emitter will have P(1) = 1, which means the source emits exactly one photon.

6.5 Indistinguishability and Purity

The future of quantum technology by the use of single-photon emitters may require indistinguishability. This means photons emitted from a single-photon source are emitted into the same quantum state. The indistinguishability of two photons can be defined from their density matrices

$$\Gamma(\hat{\rho}_1, \hat{\rho}_2) = 1 - \frac{1}{2}||\hat{\rho}_1 - \hat{\rho}_2||^2 \tag{6.9}$$

This gives an upper limit of one when the two states are indistinguishable, $\hat{\rho}_1 = \hat{\rho}_2$, and a lower limit of zero when they are perfectly distinguishable. The purity of the state can be written as

$$P = Tr\{\hat{\rho}^2\} \tag{6.10}$$

where purity has an upper limit of one for a pure state, and 1/N for a mixed N-dimensional state. The purity of the state is important for indistinguishability.

6.6 Single-Photon Emitters in Silicon

Recent research have shown single photon emitters in carbon implanted silicon [17]. Durand et al. investigated the near-infrared range and found seven single-photon emitters from different optically active point defects in silicon. Their PL spectra is shown in figure 6.3 The single-photon sources (SD-1 to SD-6 and

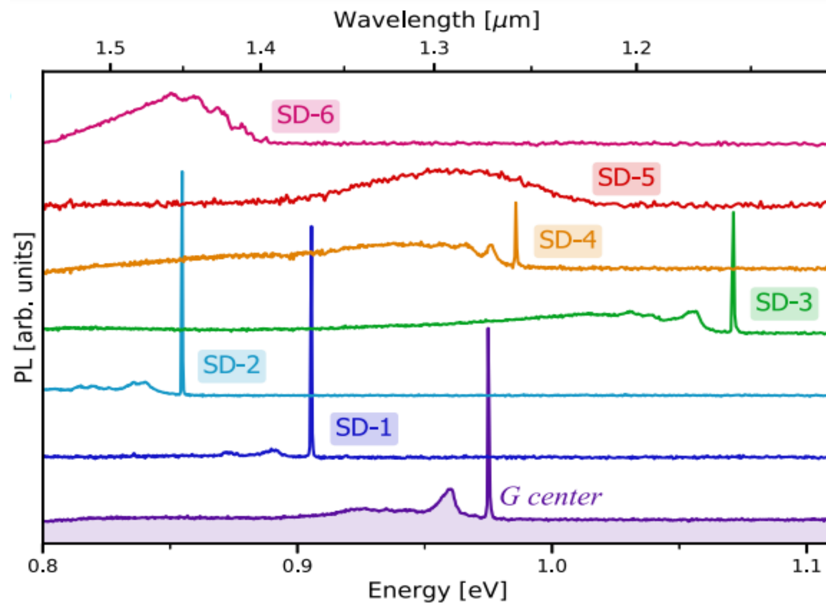

Figure 6.3: PL spectra on seven individual single-photon emitters as a function of energy below and wavelength above. Figure copied with permission of author [17]

the G center) show strong antibunching and their second order coherence fulfills the single photon criteria $g^{(2)}(0) < 0.5$.

Chapter 7

Material Properties of Silicon

This chapter is based on Streetman [39], Yang [43], Auslender [7] and Yoshida [44].

7.1 Growth

Silicon is one of the most abundant elements on earth. Pure silicon is not found in nature, but is found in combination with oxygen (SiO_2 - silica) and other elements (Al, Mg, Ca, Fe, etc - silicates). To grow very pure silicon used in the electronics industry, silicon dioxide is reduced by carbon in the form of coke in a furnace (∼1800°C)

$$SiO_2 + 2C \longrightarrow Si + 2CO \tag{7.1}$$

The result is metallurgical grade silicon (MGS) which contain high levels of impurities such as Fe, Al and heavy metals (∼100-100 000 ppm). The MGS is then refined to yield electronic-grade silicon (EGS) by reaction with dry HCl.

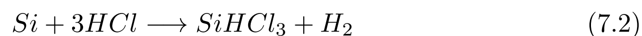

$$Si + 3HCl \longrightarrow SiHCl_3 + H_2 \tag{7.2}$$

The resulting trichlorosilane is a liquid with boiling point of 32°C. The other chlorides formed with the impurities have different boiling points than $SiHCl_3$. This is then heated and distilled using different distillation towers with distinct temperatures which separate the trichlorosilane from the other chlorides. Then $SiHCl_3$ is changed into highly pure EGS with impurities in the ppb range:

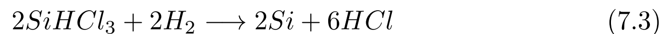

$$2SiHCl_3 + 2H_2 \longrightarrow 2Si + 6HCl \tag{7.3}$$

This polycrystalline EGS can be converted into single-crystal ingots by the use of the Czochralski method. Here the EGS are molten and a seed crystal is lowered into the melt. The seed is then slowly raised and the crystal is allowed to grow from the seed and the resulting ingots are usually grown in the <100> direction. Then the ingots are mechanically grinded into cylinders before they are sawed into individual wafers using a saw containing diamond. The final steps before the wafers are done is marking, lapping (make it flat), etching, polishing, cleaning and inspection.

7.2 Crystal Structure

Silicon is the 14th element of the periodic table and has electron configuration [Ne]$3s^23p^2$. It can complete its octet by forming sp^3 hybrid orbitals, sharing electron pairs and thereby forming covalent bonds with four neighbouring atoms. The crystal structure of silicon is the diamond structure. This structure is a face centered cubic (fcc) lattice with an extra atom placed at a/4 + b/4 + c/4 from each atom of the fcc lattice as seen in figure 7.1 Even though all the atoms

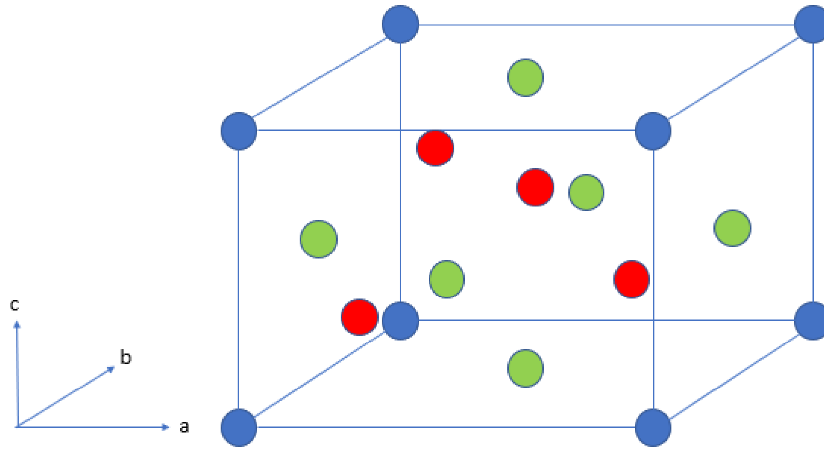

Figure 7.1: Cubic (blue), fcc (blue + green) and diamond crystal structure (blue + green + red). Colours are for illustrative purposes.

from the fcc lattice have en extra atom at a/4+b/4+c/4, only four of them are in the unit cell (marked red). The rest of the extra atoms will have positions outside, i.e. in the cells around.

7.3 Impurities and Defects

Impurities and defects can add extra energy levels in the band gap of the material. Table 7.1 shows some common impurities and their energy levels in silicon. The rest of this section is dedicated to some of the majority impurities and defects in silicon and is based upon Yang [43].

7.3.1 Oxygen

Oxygen is one of the most abundant impurities in silicon. This is mainly because highly pure silicon is extracted from materials containing oxygen (quartz, silicates, etc.). The concentration of oxygen impurities ranges typically between 10^{17}-10^{18}cm^{-3}. Interstitial oxygen diffuses slowly compared to metals and intrinsic point defects. Heat treatment of silicon (~350-500°C) can generate thermal donors (TD), which are shallow donor centers consisting of chains of oxygen molecules as seen in figure 7.2. High interstitial concentration of oxygen increase the formation of TDs, while high concentration of vacancies inhibit this formation.

Impurity	Donor/Acceptor	Below E_C (eV)	Above E_V (eV)
Ag	D	0.310	
	A		0.210
Al	A		0.057
As	D	0.049	
Au	D		0.330
	A	0.540	
B	A		0.045
Cu	A		0.490
	D		0.240
Fe	D	0.550	
	D		0.400
Ga	A		0.065
In	A		0.160
Li	D	0.033	
Mn	D	0.530	
P	D	0.044	
Sb	D	0.039	
S	D	0.180	
	D	0.370	
Zn	A	0.550	
	A		0.300

Table 7.1: Energy levels of impurities in silicon [7]

Interaction with Vacancies

The strain on the precipitates can be relieved by absorbing a lattice vacancy or the ejection of a silicon self interstitial, which will form secondary defects or diffuse away. This means that vacancies enhance oxygen precipitation while self interstitals inhibits it.
In Cz silicon, the vacancy concentration is usually about 0.5-1.0$\times 10^{12}$cm^{-3}. The vacancies can form VO_n complexes with oxygen and the VO_2 complex is assumed to be most dominant.

Interaction with Carbon and Nitrogen

Interstitial oxygen can trap interstitial carbon and thereby forming C_iO_i complexes which enhance precipitation. These complexes are electrically active defects. Nitrogen is worth mentioning when talking about oxygen as well, as it is also known as an oxygen precipitation enhancer.

Interaction with Boron and Hydrogen

Both Boron and Hydrogen increase the diffusivity of oxygen in silicon. This then bring about oxygen precipitates. Boron can also form some metastable complexes with oxygen while hydrogen can act as a catalyzer in the forming of thermal donors.

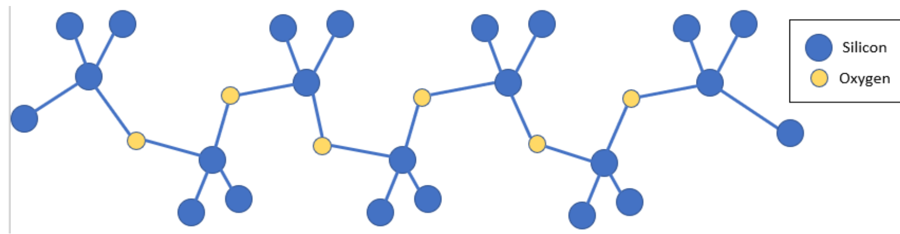

Figure 7.2: Thermal donor given by a chain of oxygen atoms

7.3.2 Carbon

Carbon is used to reduce silicon in the Czochralski process and this causes it to be another of the major impurities in silicon. Carbon in silicon can either take the form of substitutional or interstitial and can form a variety of complexes. Carbon in silicon precipitates into silicon carbide particles if the concentration surpass the solubility limit. The electronically active G center is a complex of two substitutional carbon atoms and an interstitial silicon atom.

7.3.3 Nitrogen

Of the light elements, nitrogen is one of the most common impurities in silicon. From earlier sections nitrogen was an enhancer for oxygen precipitation but it also increases the mechanical strength of silicon. It exists as monomers, dimers or complexes is silicon. Many defect complexes containing nitrogen are formed from its reaction with other constituents. These reactants can be interstitial and substitutional nitrogen and silicon, vacancies, or other impurity atoms and the structure of the defects influences the thermal stability and its vibrational modes.

7.3.4 Metal Impurities

Co, Cr, Fe, Zn and Ni have concentrations above 10^{12}cm^{-3} in silicon. Only a small fraction of them are electronically active and that's because most of them precipitate or aggregate at extended defects such as dislocations. The excess carrier recombination rate of silicon is greatly enhanced by metal impurities and extended defects. Doping silicon affects the charge of the metal impurities and positively charged substitutional metal impurities dominate in p-type while negatively charged substitutional impurities dominate in p-type. The 3d transition metal impurities in silicon is are some of the fastest diffusing species. Silicons diamond crystal structure is fairly open, and this is favourable for interstitial impurities.

Iron

Iron in silicon is unstable in the substitutional form and inhabits the interstitial Fe_i position, complexes with other defects or precipitates. It can form bonds with other impurities such as boron in p-type silicon. Interstitial iron has a donor level at $E_{Fe_i} = E_V + 0.39$ eV whereas the iron-boron (FeB) pair has two energy levels: donor at $E_t = E_V + 0.09$ eV and acceptor $E_t = E_C - 0.29$ eV.

Nickel

Nickel forms silicides in silicon at elevated temperatures. The diffusion mechanism for nickel in silicon is usually via interstitial sites. It is neutral at interstitial sites and has no effect on the electrical properties of silicon. Complexes with other defects however, show energy levels in the band gap. An example is nickels interaction with vacancy-oxygen centers that have shown to give an energy level at E_C -0.37 eV. Nickel's fast diffusion at room temperature allows it to diffuse to surfaces, precipitate or react with other defects.

Copper

As opposed to nickel, interstitial copper is positively charged thereby exhibiting a shallow donor level in the upper half of the band gap. It is also stable in the substitutional position Cu_{Si} and yields three main energy levels: E_C - 0.017 eV, E_V + 0.430 eV and E_V + 0.225 eV. These levels are usually designated to the double-acceptor, single-acceptor and single-donor states, respectively. Copper also forms complexes with other impurities and defects. One of them is the defect center with a substitutional Cu_{Si} surrounded by three interstitial Cu_i which gives a donor level at E_V + 0.1 and a ZPL at 1.014 eV. Only a small fraction of the total Cu concentration in silicon form electrically active point defects and complexes. Dislocation-precipitate colonies are formed because of the lattice mismatch between Cu silicides and silicon, causing stress. The stress leads to dislocations which again can lead to new precipitation of Cu and Si.

Chromium

Chromium can occupy both interstital Cr_i and substitutional Cr_{Si} positions. Cr_i are electrically active defects and has donor level at E_C - 0.23 eV. In p-type silicon, chromium forms bonds with boron (CrB) and these have donor level at E_V + 0.28 eV. As with iron, these pairs can be disassociated by adequate energy but will pair up again after some time when the energy is removed.

Cobalt

Cobalt is found in concentrations much lower than iron, nickel and copper and is the lightest of the high diffusivity metals mentioned. Because of its fast-diffusing nature at room temperature, Co_i are not anticipated by itself but has been observed in complexes with other impurities and defects. Substitutional cobalt, Co_{Si}, have acceptor level at E_C - 0.39 eV and the acceptor level at E_V + 0.46 eV have been linked to the defect center of the Co_iB_{Si} pair. Co_iCo_{Si} pairs form defect centers which are electrically inactive.

Titanium

Titanium in the interstitial position is electrically active and two energy levels are ascribed to it: E_C - 0.09 eV (single-donor) and E_V + 0.25 eV (double-donor). Substitutional titanium, Ti_{Si}, has a single-acceptor state at energy level E_C - 0.28 eV and both substitutional and interstital titanium are powerful recombination centers.

7.3.5 Vacancies

Vacancies and interstitials are some of the most dominant defects in silicon as it lowers the Gibbs free energy of the material. Irradiation by ions cause elastic collisions between the highly energetic ions and host atoms. If the energy transfer in these collisions are over a certain threshold value, the host atoms will move into interstitial positions leaving behind an empty spot. After irradiation, the defects created move about the material and either recombine or get captured by other defects or impurities to lower their energy. Of the small fraction who survive this migration and recombination, some of the most common defect complexes are the divacancy (V_2) and the vacancy oxygen pair (VO) [41].

7.4 G-line

The G center (1269nm) has earlier been identified as a common defect complex consisting of a interstitial silicon atom surrounded by two substitutional carbon atoms [14] as seen in figure 7.3

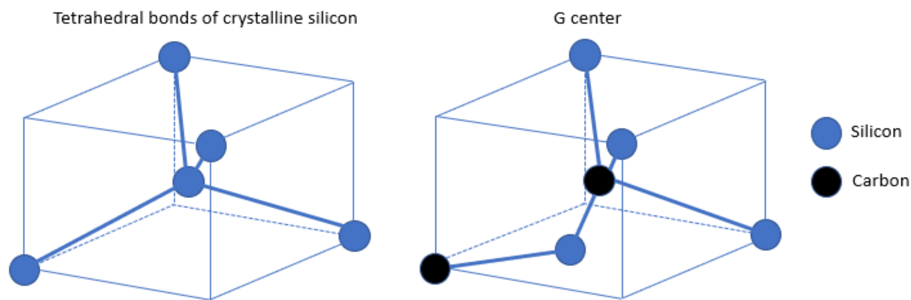

Figure 7.3: Crystalline silicon (left) and the G center (right)

7.5 W-line and X-line

The W-line at 1218nm in silicon has been reported numerous times and believed to be a small interstitial cluster of Si atoms [20, 27, 11, 1]. Giri showed that the W center is a result of migrating defects that form stable interstital clusters by depth profiling and PL measurements [20]. He also found that a X-line at $\sim$ 1200nm forms at the cost of the W-line, meaning this is a bigger cluster of silicon interstitials that uses the smaller clusters of the W-line as a building block. The W-line also has a phonon replica at 1244nm called W'.

7.6 C-line and P-line

The C-line at 1616nm is be attributed to interstitial carbon-interstital oxygen (C_iO_i) complex [34]. The P-line at 1570nm is attributed to a carbon-oxygen complex [35, 12]

Chapter 8

Quantum Technology

This chapter will give a brief introduction to quantum technology and the possibilities for use of single-photon emitters in future technologies. Based on Bathen [8], Griffiths [21], O'Brien [30] and Dreyer et al. [16].

8.1 Important Principles of Quantum Physics

8.1.1 Heisenberg Uncertainty Principle

The Heisenberg uncertainty principle states that the position and momentum of a particle can only be measured up to a certain accuracy

$$\Delta x \Delta p \geq \frac{\hbar}{2} \tag{8.1}$$

meaning it is impossible to know both position and momentum at the same time. Quantum physics therefore uses probability to describe the position of a particle instead.

8.1.2 Superposition

In quantum mechanics, electrons are treated as waves inhabiting quantum states. These states can be expressed by a sum of other well-defined states and this is whats called superposition as illustrated in figure 8.1 The observer effect is when

Figure 8.1: Illustration of superposition

measuring a quantum system forces the system into one of the states of the superposition. So the act of measurement has destroyed the possibility for the system to be in its other states. In other words, if there is a possibility a system

can be in various different arrangements, then the actual state of the system is a combination of these possibilities. It is only when the system is observed that this breaks down and the system goes into a distinct arrangement.

8.1.3 Entanglement

Quantum entanglement is a phenomenon of particles or groups of particles in quantum states that cannot be described independently of each other. If the state of one particle is known, the state of the other or others can be deduced since they are correlated as illustrated in figure 8.2

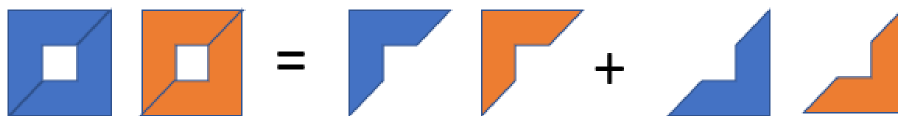

Figure 8.2: Illustration of entanglement

8.1.4 Coherence and Decoherence

Because of the wave-like properties of particles and matter, interference occur and phase relations between quantum states are created. This is whats called coherence and is related to superposition and entanglement. For a system to to be coherent, it must be isolated from its environment and loss of the phase relation is called decoherence.

8.2 Quantum Sensing

Since quantum systems are extremely sensitive to perturbations from the environment, they are subject to decoherence. Quantum sensing aims to utilize the systems response to minuscule alterations. The quantum system is prepared in a certain state and changes in the state from physical properties (temperature, fields, etc.) are measured.

8.3 Quantum Communications

Quantum communication aims to transfer information from one location to another by means of quantum states. Several methods have been theorized to carry out this task. Entanglement is one since the quantum states of one system will affect the states of another even though there is a distance between them. Photons prepared in a certain state is another, since the decoherence can be low in optical cables.

8.4 Quantum Computing

Classical computers have continued to enhance their processing power through the years as per Moore's law [26]. This predicts that transistors on integrated circuits decrease in size by approximately 50% every two year, thereby doubling

the transistor count on each circuit. Transistors function by electrical signals and resistivity and eventually the size will be so small that there will be too few atoms to cause any resistance. As we approach this limit, quantum computers have become a viable solution to keep increasing processing power.

8.4.1 Qubit

Classical computers use transistors and tiny electrical signals for their logic. These switches are labeled 0 (OFF) if they inhibit current and 1 (ON) if current can flow through. Quantum computers use quantum bits (qubits) for their logic and these can exist in a superposition of the two states as illustrated in figure 8.3. Potential systems for generation of qubits exists in a variety, but the focus of this chapter will be on single photons as qubits.

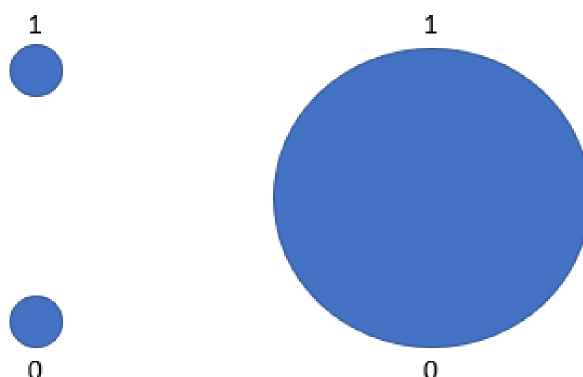

Figure 8.3: Illustration of the two level system of a classical bit (left) and quantum bit (right)

8.4.2 Requirements for Quantum Computing

For a quantum computer to be usable and functional there are some requirements to the system set by DiVicenzio [15]:

1. Be scalable with well characterized qubits
2. Have a standard fixed state for the qubits to initialize
3. Long decoherence times compared to the gate operation time
4. A set of "universal" quantum gates
5. Possibility to read the qubits

Defects in silicon have some isolation and therefore decoherence times that are longer than several other systems. They can also be discrete two-level systems which are initialized by optical absorption. When it comes to scalability, silicon is one of the most researched materials in the world and much is known about the defects and their formation mechanisms.

8.4.3 Optical Quantum Computing

Optical quantum computing is feasible using single-photon sources, linear optical elements and single-photon detectors [30]. A possible realisation of the qubit is by the polarization of a single photon as seen in figure 8.4 The polarization

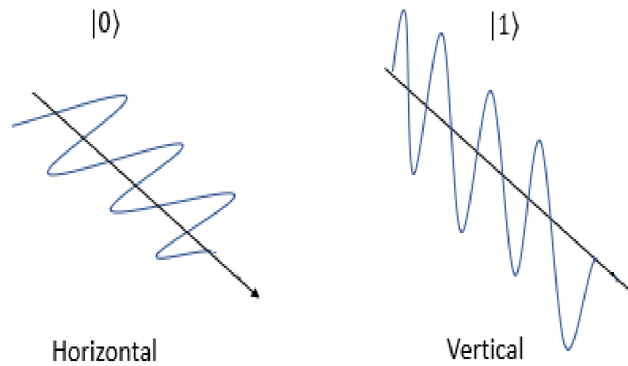

Figure 8.4: Horizontal (H) and vertical (V) polarization of a single photon [30]

of the photon give the two states ($|0\rangle \equiv |H\rangle$ and $|1\rangle \equiv |V\rangle$) and these states represent a logical "0" or "1", respectively. A state of the qubit is given by $\alpha|H\rangle+\beta|V\rangle$ where α and β are complex numbers who satisfy $|\alpha|^2 + |\beta|^2 = 1$, and can be illustrated on the Bloch sphere in figure 8.5. The states that are

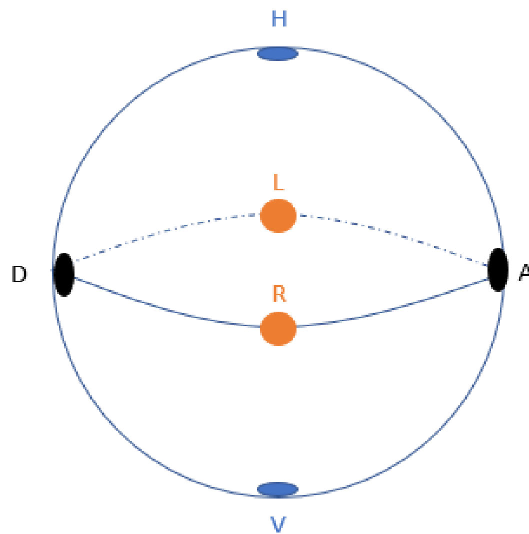

Figure 8.5: Bloch sphere with some marked states [30]

shown in figure 8.5 are; $|D\rangle \equiv |0\rangle+|1\rangle \equiv |H\rangle+|V\rangle$, $|A\rangle \equiv |0\rangle-|1\rangle \equiv |H\rangle-|V\rangle$, $|L\rangle \equiv |0\rangle-i|1\rangle \equiv |H\rangle-i|V\rangle$ and $|R\rangle \equiv |0\rangle+i|1\rangle \equiv |H\rangle+i|V\rangle$. Birefringent wave plates can be used to make gates because they delay one polarization relative to the other, causing a rotation of the Bloch sphere. The rotation is determined by the inclination of the wave plates. A great example is the Hadamard gate which

has the logic: $|0\rangle \rightarrow |0\rangle$+$|1\rangle$ and $|1\rangle \rightarrow |0\rangle$-$|1\rangle$ which can be written $|H\rangle \rightarrow |D\rangle$ and $|V\rangle \rightarrow |A\rangle$. A random rotation of the state would require a different sequence of the birefringent wave plates and both gates are shown in figure 8.6.

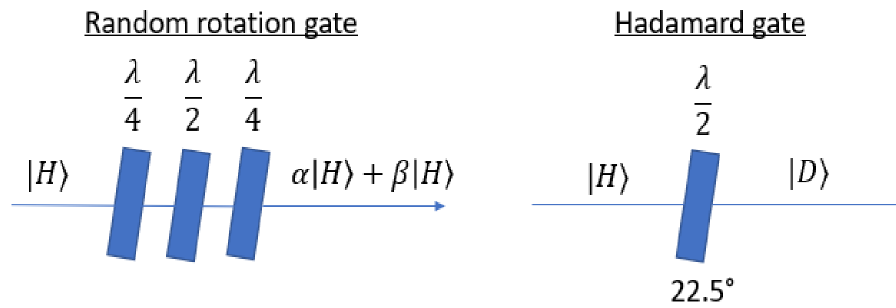

Figure 8.6: Illustration of the random rotation gate and the Hadamard gate [30]

Part III

Methodology

Chapter 9

Proton Irradiation

The following chapter is based on Bathen [8], Streetman [39] and Pellegrino [31].

9.1 Sample Preparation

The samples were cut into 0.8cm x 0.8cm squares by using the laser cutter at the Norwegian Micro - and Nano Fabrication Facility (Minalab). The laser used was the Rofin scribing laser (Model: PL E 25 SHG CL Flex, Manufacturer: Roffin) which is intended for scribing and cutting. The parameters used to cut the wafers are given in table 9.1 and both n- and p-type silicon with thickness 500 μm were used and marked 1, 2, 3 and 4 (n-type) and 19, 20, 23, 22 (p-type). The n-type were phosphorus doped with resistivity 5-10 $\Omega\cdot$cm and the p-type were boron doped with 1-5 $\Omega\cdot$cm resistivity. The samples were then cleaned using isopropanol in a ultrasonic bath for 15 minutes, then rinsed in distilled water before being dried by N_2.

Current (A)	32
Frequency (Hz)	50000
Speed (mm/s)	200
Execution count	130

Table 9.1: Laser parameters

9.2 Proton Irradiation

The silicon samples were irradiated with 1.8 MeV hydrogen ions in fluences given in table 9.2. The irradiation was done using the NEC Tandem accelerator at the Norwegian Micro - and Nano Fabrication Facility (Minalab). The ions were accelerated to kinetic energies of choice and then directed to at the samples as seen in the illustrative setup of figure 9.1 The point of the irradiation is to create defects in the silicon samples and see if there are any trends to the different irradiation fluences. The distribution of the ions in the sample after irradiation is dependent on the energy and mass of the ions and also the beams angle when directed at the surface. Since the collisions are random, the distribution of the

n-type	Fluence (ions/cm^2)
1	$5{\times}10^{10}$
2	$5{\times}10^{12}$
3	$5{\times}10^{14}$
4	$5{\times}10^{16}$
p-type	
19	$5{\times}10^{10}$
20	$5{\times}10^{12}$
23	$5{\times}10^{14}$
22	$5{\times}10^{16}$

Table 9.2: Fluence details

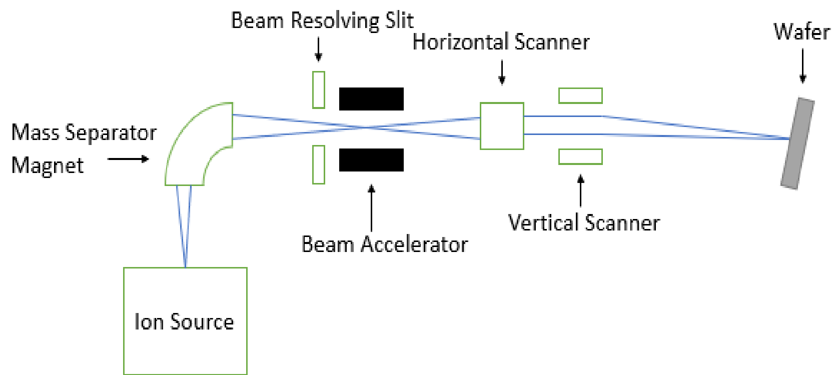

Figure 9.1: Basic setup for ion irradiation

ions will have an approximately Gaussian curve around some projected range (R_p) which depends on the energy and ion mass. The distribution of ions with an implanted dose ϕ ions/ cm^3 will be

$$N(x) = \frac{\phi}{\sqrt{2\pi}\Delta R_p} exp\left[-\frac{1}{2}\left(\frac{x - R_p}{\Delta R_p}\right)^2\right] \tag{9.1}$$

where both R_p and ΔR_p is dependent on the implantation energy.

Chapter 10

Optical Characterization

This chapter is based on Berhanuddin [18], Heinz [22] and Fuchs [19].

10.1 Photoluminescence Spectroscopy

The optical properties of the samples manufactured in this work have been studied by steady-state photoluminescence (PL). PL is a contactless characterization technique that can provide valuable information about the surface and bulk recombination processes of a semiconductor. At room temperature carriers

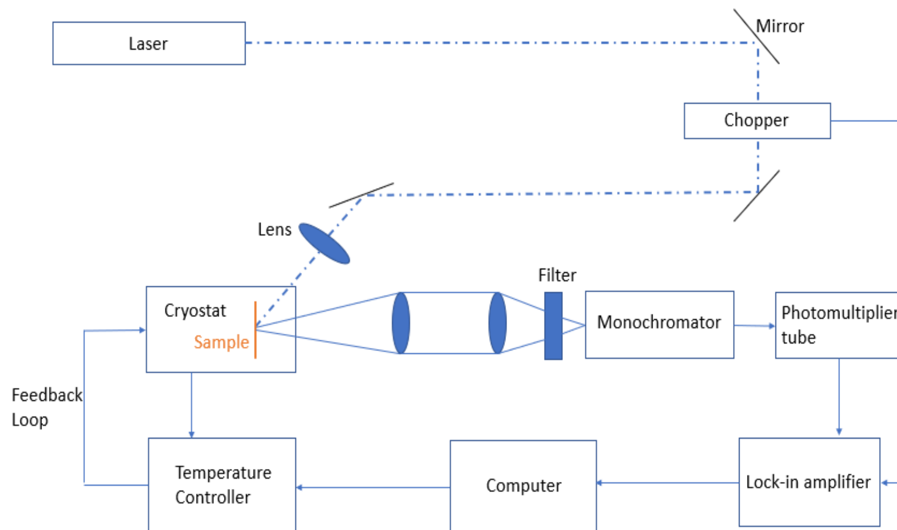

Figure 10.1: Illustration of photoluminescene spectroscopy setup

can thermally escape to higher energy levels, and therefore have enough energy to get to non-radiative recombination centers, which translate into a strong reduction of the intensity of the PL signal. I addition, at room temperature there is an increase in the exciton (electron) - phonon interactions. This leads to a sizeable broadening of the photoluminescence bands and the overlapping of bands with close energies. Therefore, it will make it difficult to analyze the

structure of the photoluminescence spectra. Consequently, we have performed our measurements at 4K to reduce the likelihood of non-radiative recombination. The PL was measured using a standard setup as shown schematically in figure 10.1. The samples were placed into a closed-cycle He-refrigerator and excited using fixed continuous wavelength-lasers. Two lasers were used during the pretests and their absorption depth in the material vs wavelength of laser is shown in figure 10.2 The way the samples were irradiated makes the defects

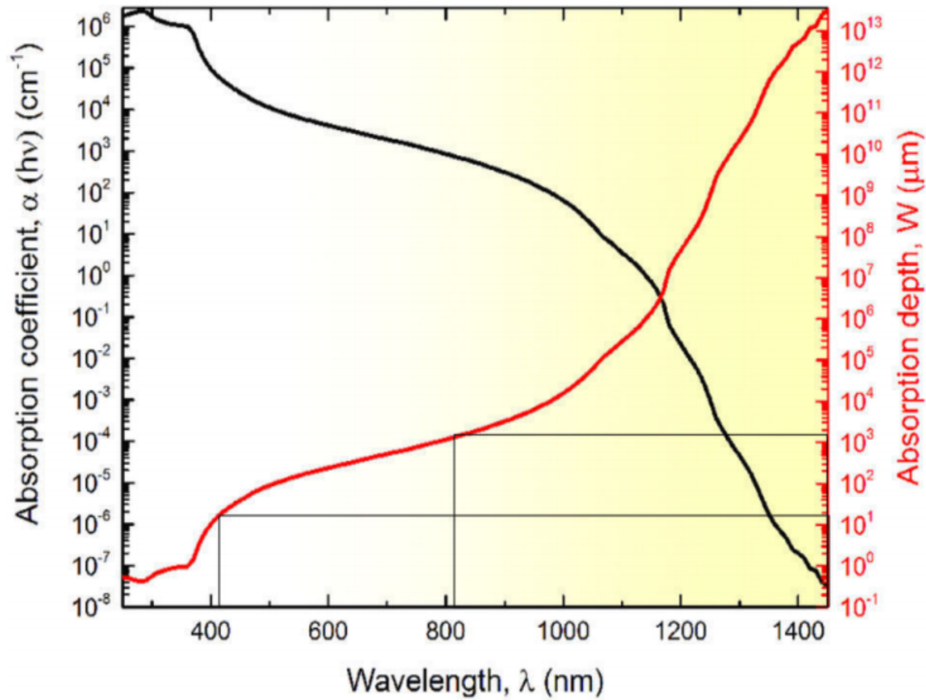

Figure 10.2: Absorption depth vs laser wavelength

shallow (which is seen in the SRIM analysis later) and the 405nm laser were chosen instead of the 804nm as so the results would not yield spectra of bulk silicon. The emitted PL was collected using NIR microscope objectives that cover a wide range of wavelengths from visible to infrared. The spectra were recorded using a UV-VIS-NIR photomultiplier tube, which is sensitive from 330nm to 1800nm. A band-pass filter was placed in front of the photomultiplier to prevent unwanted radiation. The PL spectrum has been done with a step of 0.1nm and an acquisition time of 1s per wavelength. Finally, a lock-in amplifier was used in order to improve the signal-to-noise ratio. The photoluminescence spectrum were found by evaluating the intensity of the emitted photons as a function of their wavelength.

Chapter 11

Electrical Characterization

This chapter is based on the Ph.D's of Vines [41] and Pellegrino [31] and also the DLTS introductory script of Karsthof, Bathen and Bonkerud [9].

11.1 Capacitance measurements

Capacitance measurements were done on the samples first to see if they were suitable for DLTS measurements. To make the rectifying junction, aluminum and gold where deposited on p- and n-type, respectively. A silicon wafer with laser-cut circular holes with diameter of 1.2mm were used as a mask to make the metal contacts and the back contact was achieved by applying silver paste on the back of the samples. For the CV measurements the samples were approximated to be plate capacitor with capacitance

$$C = \frac{\epsilon A}{W} \tag{11.1}$$

where A is the area, ϵ the dielectric constant of silicon and W the depletion region. The capacitance of the samples were measured at room temperature between 0 and -5V and the built in voltage was thereby found from extrapolation of the $1/C^2$ curves and the carrier concentration (doping concentration, N_d) from its derivative

$$\frac{1}{C^2} = \frac{2(V_0 + V)}{A^2 q \epsilon N_d} \Longleftrightarrow N_d = \frac{2}{A^2 q \epsilon \frac{d \frac{1}{C^2}}{dV}} \tag{11.2}$$

The carrier concentration extracted from the CV measurements gives a doping profile and is also used with DLTS measurements to give the concentration of defects. The diode area was set to 1.13E-2 cm^2 while ϵ for silicon was set to 11.7.

11.2 DLTS

11.2.1 Principles of Operation

This chapter will refer to n-type, but the same relations can be obtained for p-type by swapping the roles of electrons and holes. DLTS operates by changing

the width of the depletion region by applying a voltage. In a Schottky contact the depletion region is

$$W = \sqrt{\frac{2\epsilon}{qN_d}V_r} \tag{11.3}$$

Without bias, the depletion region is depleted of carriers. When a forward pulse is applied the depletion region width is decreased and a certain fraction of the defects in the steady-state depletion region capture charge carriers. The effective doping concentration in W after removing the pulse is

$$N_d^{eff} = N_d - n_t(t) \tag{11.4}$$

where $n_t(t)$ is the concentration of filled electron states after the pulse is removed

$$n_t(t) = N_T e^{-e_n t} \tag{11.5}$$

and N_T is the concentration of the defect states. After removing the pulse bias the defect level is now above the Fermi level in certain parts of the depletion region, which will make it emit charge carriers thermally. This causes the time-dependent capacitance

$$C(t) = A\sqrt{\frac{q\epsilon N_d^{eff}}{2V_r}} \tag{11.6}$$

The assumption that the concentration of defects are much less than the dopant concentration ($N_T << N_d$) yields

$$C(t) = C - \Delta C(t) \tag{11.7}$$

where

$$\Delta C(t) = \frac{CN_T}{2N_d}e^{-e_n t} \tag{11.8}$$

Since the emptying of the states after pulse removal depend on temperature, the process goes faster with increasing temperature and DLTS spectrum is obtained measuring capacitance transients as functions of temperature as seen in figure 11.1. This figure is for illustration purposes only as it uses the so-called "boxcar" correlation function for its weighting function w(t). The setup used in this thesis has the lock-in function, the GS-2 correlation function and the GS-4 correlation function. The DLTS signal is

$$S(t_i) = \frac{1}{t_i}\int_{t_d}^{t_d+t_i} \Delta C(t)w(t)dt \tag{11.9}$$

where t_d is a delay time. There is a unique relation between the rate window and the actual emission rate, which depend on the choice of correlation function and time constants t_d and t_i, which gives $S(t_i)$ its maximum. Another important relation is the one between S_{max} and the defect concentration N_T given in equation 11.10

$$S_{max} = F_i C\frac{N_T}{N_d} \tag{11.10}$$

where F_i is a factor that is determined by the rate window used. So by knowing S_{max}, N_T can be calculated. Changing the time window t_i give different values of the rate of emission, e_n, for different temperatures and

$$e_n(T) = v_{th}\sigma_n N_C e^{-\frac{E_T}{kT}} \tag{11.11}$$

give E_T and σ using an Arrhenius plot.

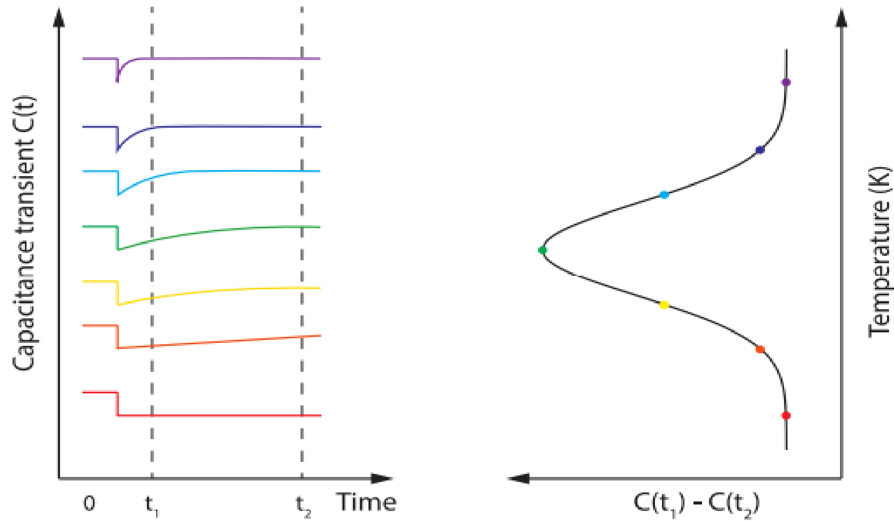

Figure 11.1: Illustration of how a DLTS spectrum can be obtained. Left shows C + ΔC(t) at different temperatures and the right is the constructed DLTS signal given by C(t_1)-C(t_2) as a function of temperature [9].

11.2.2 Method

The samples where glued in place with silver paste in a vacuum chamber and cooled down to $\sim$ 25K before being slowly heated 2K/min to 300K during measurement. The bias voltage were -5V and the pulse voltage 5V on the samples. The capacitance measurements were done with the use of the Boonton 7200 Capacitance Meter in the range of 200 pF which gives an accuracy of 0.25% of reading + 0.2% of range + 0.005 pF. The apparatus measured all the transients and conductances for different temperatures while the DLTS signals was calculated by the program and all this was stored in text files.

In order to extract defect properties such as their activation energy, apparent capture cross section and concentration, a simulation tool was used, which was created by former Ph.D student at the University of Oslo, Christian Zimmermann. This tool assumes the existence of a set of traps with which the values of the above parameters are freely chosen by the user. The script generates artificial capacitance transients based on that set of defects, and calculates corresponding DLTS spectra (different correlation functions can be employed). By adjusting the parameter values one by one, the measured spectra are reproduced as good as possible, and the resulting parameters set is assumed to reflect the samples defect population. From this one could read out the information about the different defects and try to match them to literature. For n-type longitudinal effective mass of 0.98m_0 was used, while for p-type an average of heavy and light holes was set to be 0.34m_0.

Chapter 12

Four-Point Probe Measurement

The four-point probe is a method to determine the resistivity of a sample. This strategy reduces the effect of contact resistance at the measuring points by sending current through two outer probes and then measuring the voltage in two inner probes. An illustration of the setup is shown in figure 12.1 The

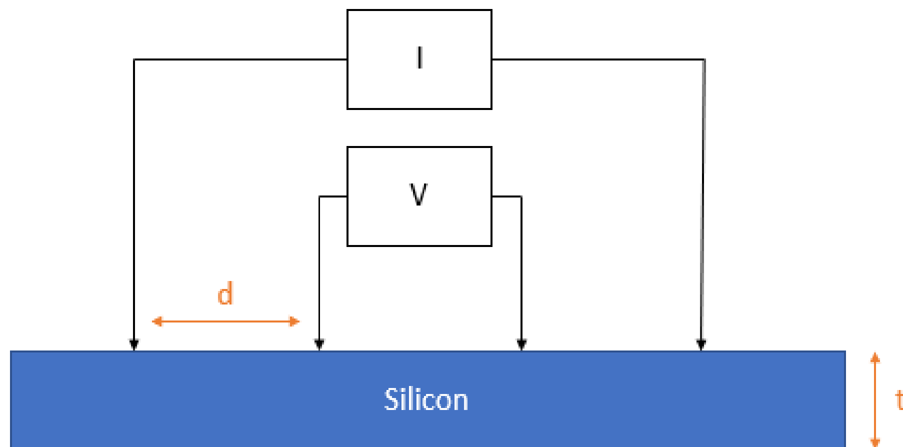

Figure 12.1: Four-Point Measurement Setup

resistivity is given by

$$\rho = C_1 C_2 \frac{V}{I} t \tag{12.1}$$

where C_1 and C_2 are correction factors that relate the distance between probes to the diameter of the wafer and to the thickness of the sample. The majority carrier concentration can then be calculated assuming full ionisation

$$\frac{1}{\rho} = q(n\mu_n + p\mu_p) \tag{12.2}$$

Part IV

Results

Chapter 13

Simulation of Ion Impacts

SRIM (Stopping and Range of Ions in Matter) simulation for 10 000 1.8 MeV hydrogen ions implanted in a 500 μm thick silicon wafer, yielded the vacancy distribution given in figure 13.1 The number of vacancies produced is dependent

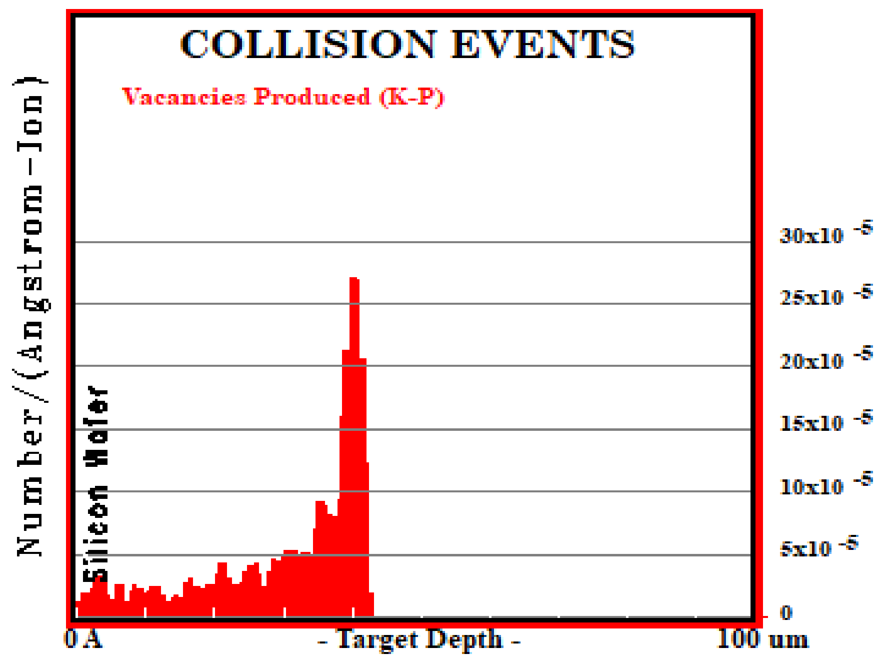

Figure 13.1: Depth profile of vacancy distribution

on depth and taking the average number to be 5x10^{-5}/(Angstrom-Ion) gives

$$5 \times 10^{-5}/\AA - Ion = 5000/cm - Ion \tag{13.1}$$

starting with the first implantation fluence of 5x10^{10} this gives a vacancy concentration

$$[v] = 5 \times 10^{10} Ion/cm^2 \cdot 5000/cm - Ion = 2.5 \times 10^{14}/cm^3 \tag{13.2}$$

The rest of the vacancy concentrations for the different fluences is given in Table 13.1 The concentration will of course vary by depth in the material since the

n-type	Fluence (ions/cm^2)	[v] (vacancies/cm^3)
1	5×10^{10}	2.5×10^{14}
2	5×10^{12}	2.5×10^{16}
3	5×10^{14}	2.5×10^{18}
4	5×10^{16}	2.5×10^{20}
p-type		
19	5×10^{10}	2.5×10^{14}
20	5×10^{12}	2.5×10^{16}
23	5×10^{14}	2.5×10^{18}
22	5×10^{16}	2.5×10^{20}

Table 13.1: Vacancy concentration vs fluence

number of vacancies created by the ions were taken as an average. It will have its maximum at about 40μm and be around 5 times larger than the values given in table 15.1. The projected hydrogen ion paths are depicted in figure 13.2 The SRIM results showed that the concentration of vacancies followed

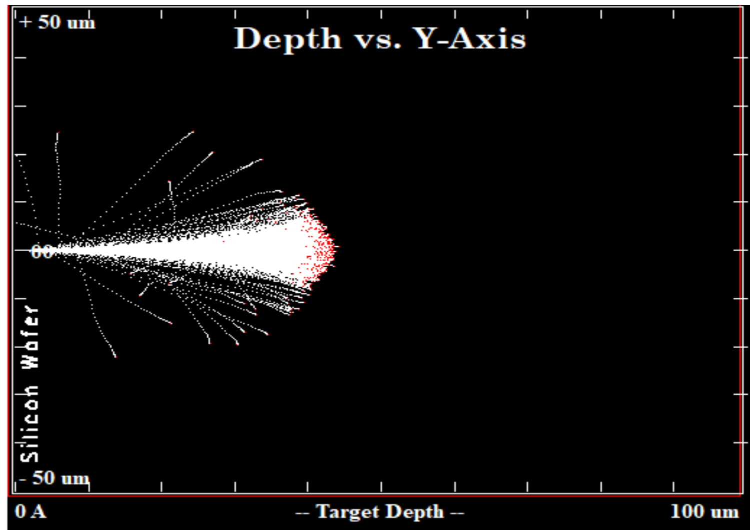

Figure 13.2: Ion penetration depth vs y-axis

a tail-like distribution with its maximum at approximately 40μm. One can assume that the probability for larger vacancy clusters, such as the divacancy, gets higher with depth (up to 40μm). The SRIM simulation does not take into account recombinations of the vacancies and the simulated value is thereby much larger than the actual value. Normally only a few percent of the vacancies and interstitials created survive recombination but SRIM analysis is still a good tool to analyse distribution and depth.

Chapter 14

Photoluminescence Spectroscopy

The PL result for the n-type silicon samples are displayed in figure 14.1 in logarithmic scale. The different optically active centers have been indicated by

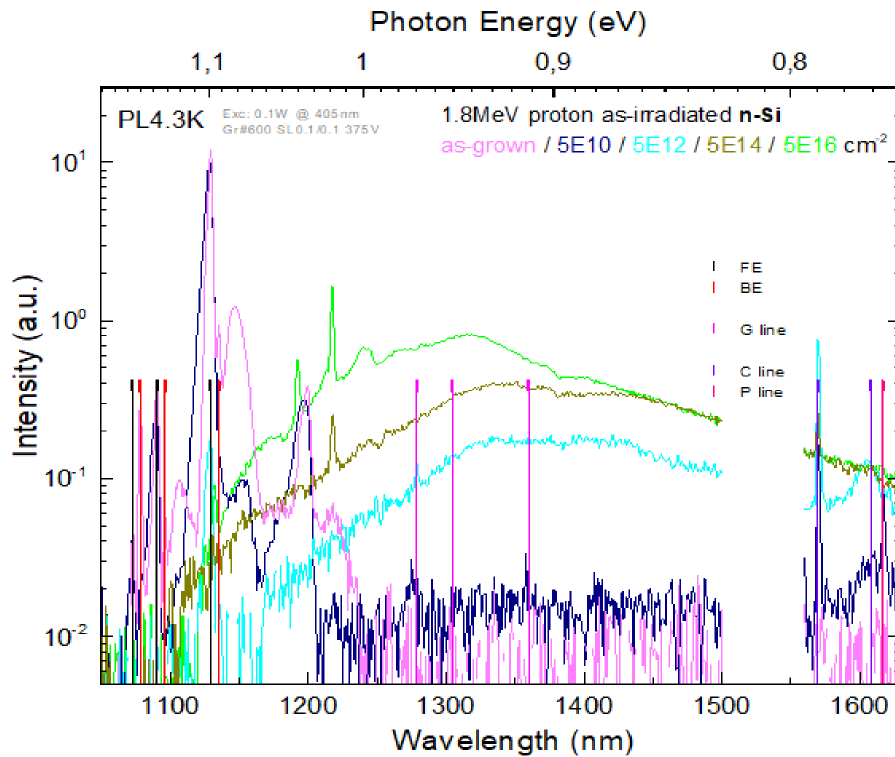

Figure 14.1: Photoluminescence spectra in log scale for n-type samples irradiated with different fluences

vertical lines. A set of PL peaks can be seen from 1050nm to 1200nm for the as grown and lowest fluence sample (5E10). These correspond to bound and

free exciton recombination which are intrinsic recombination processes, i.e. an unavoidable material property. In the samples with the highest fluence (from 5E12-5E16) the PL peaks corresponding to the excitonic recombination processes are less pronounced with increasing fluence. However, a broad NIR PL emission become more pronounced in the high fluence samples. This broad PL emission band is a consequence of the extrinsic recombination processes due to defects created by larger fluences. This increase in intensity is illustrated for both n- and p-type in figure 14.2 a) where the areas between 1200 and 1500 nm have been integrated for the different fluences. On the other hand, the PL mea-

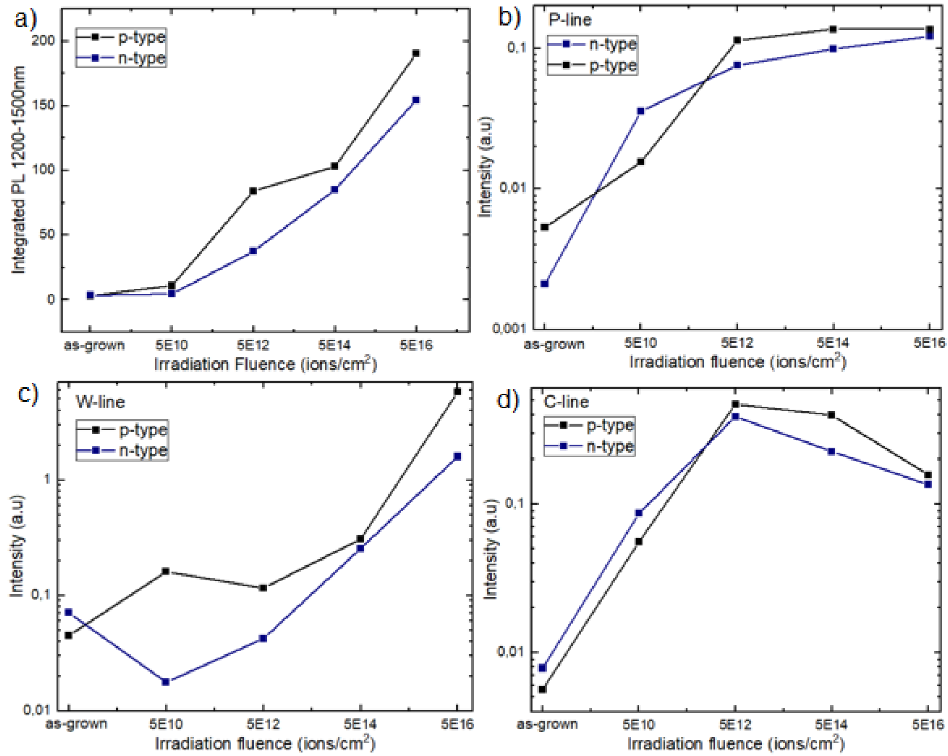

Figure 14.2: a) Integrated PL from 1200-1500 nm, b) Intensity of P-line (1570nm) vs irradiation fluence, c) Intensity of W-line (1218 nm) vs irradiation fluence and d) Intensity of C-line (1616 nm) vs irradiation fluence

surements have disclosed a set of peaks at different wavelenghts which emission intensity can be manipulated by changing the fluence. The most pronounced peaks have been observed for the sample with the highest fluence. This is an interesting result since PL sharp peaks are indication of single-photon emission. However, this can only be confirmed by photon-correlation measurements to determine the emission purity of the different peaks. The peaks are depicted in linear scale in Appendix C figure C.1 to get a better visualisation of their distinction. The most distinct peak is the W-line at 1218 nm and believed to be a cluster of interstitial silicon as mentioned in 7.5. The fact that the peak at 1192nm for 5E10 decrease with two of the higher fluences before reemerging at 5E16 further validates the theory that these two peaks are competing interstitial

clusters of different sizes (X-line also a cluster of interstitial silicon). The PL result for the p-type samples are shown in figure 14.3 in log scale while it is in linear scale for a better visualization of the peaks in Appendix C figure C.2. The intensity of the peak at 1218 nm are much larger in p- than in n-type for 5E16 and they are compared in figure 14.4. This may be caused by phosphorous acting as some kind of sink for the interstital silicon atoms in n-type or boron as a catalyst for interstital cluster formation in p-type. In figure 14.2 b), c) and d) the intensity of the P-line, W-line and C-line is illustrated in accordance to fluence. The intensity of the P-line increases with fluence and it looks like it reaches a saturation at about 5E14-5E15. The W-line increase with fluence as expected

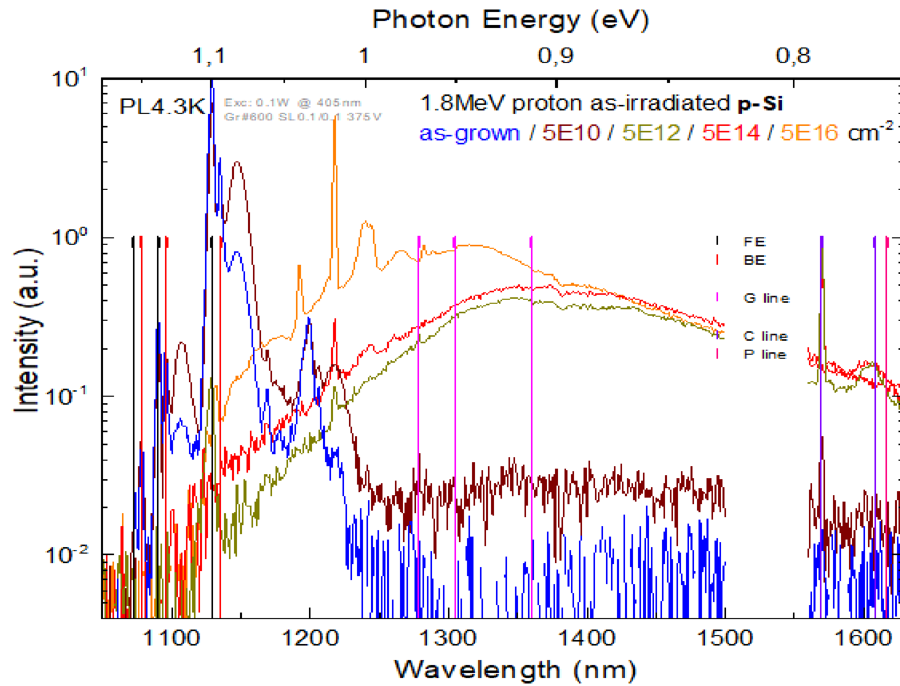

Figure 14.3: Photoluminescence spectra in log scale for p-type samples irradiated with different fluences

because higher fluence creates more interstitals for these clusters. The C-line reaches its maximum at 5E12 and decreases a bit for the two highest fluences and might be because of competing complex structures with higher irradiation fluences or because the concentration of either oxygen or carbon being depleted (C-line is C_iO_i). Marked in figure 14.4 is 5 peaks of n- and p-type with fluence 5E16 and baseline subtracted named 1 (1192nm), 2 (W-line), 3a (1239nm), 3b (1244nm) and 4 (1282nm). Only the 5E16 fluence show distinct peaks for peak 1 and 4, while peak 3a and 3b show inclinations of peaks for 5E14 also. Peak 2 (W-line) have a distinct peak for 5E12, 5E14 and 5E16 for p-type, but only for 5E14 and 5E16 in n-type. Even though most of the peaks don't show distinct peaks, their intensity is plotted dependent on the different fluences in figure 14.5. The high intensity for peak 1 at the 5E10 fluence is most likely excitons since they disappears at higher fluences. The emitted wavelength of the peaks corresponds to photons of energy 1040.14, 1000.68, 996.66 and 967.12 meV for

peak 1, 3a, 3b and 4, respectively. The band gap of silicon being ~ 1.1eV makes the defects creating these signals extremely shallow. Peak 1 is most likely the X-line discussed previously in 7.5, which is a competing cluster of interstitials silicon atoms to the W-line. Giri and Aboy also mentions that the W-line has a phonon replica at 1244 nm, which is most likely peak 3b [20, 1]. Peak 3a were inconclusive but its close proximity to 3b makes it tempting to attribute it to a phonon replica of the interstital clusters discussed earlier. The peak named "4" was found with the aid of the DLTS comparison figure 16.8 to be the vacancy-oxygen (VO) complex with an admixture of the carbon interstitial-carbon substitutional (C_iC_s) [5, 4]. Peak 4 (1282nm) being extremely close to the G center (1269±9nm) mentioned earlier in chapter 7.4 means it could also be this carbon related complex defect. The absorption depth of the laser gave approximately 20μm and this is in the middle of the vacancy distribution according to the SRIM analysis. Unfortunately the DLTS measurements took place on a depth of only a few microns and caution must be taken when comparing the two. To an approximation one can expect the defects created in the DLTS range are the same as the ones in the PL range. Even though the PL spectra did not yield any distinctive lines at the positions of SD1-SD6 as seen in Appendix C figure C.3, the results still gave some peaks at around 1200nm that might be single-photon emitters like the peaks shown in figure 14.4 with parameters given in table 14.1.

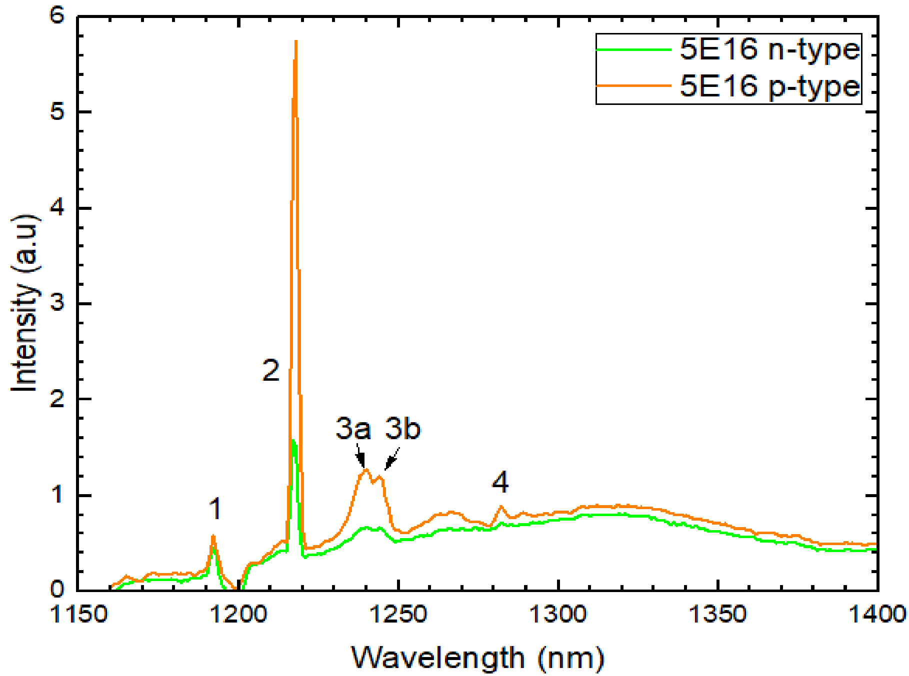

Figure 14.4: PL spectra of n- and p-type silicon with 5E16 fluence in linear scale with baseline subtracted

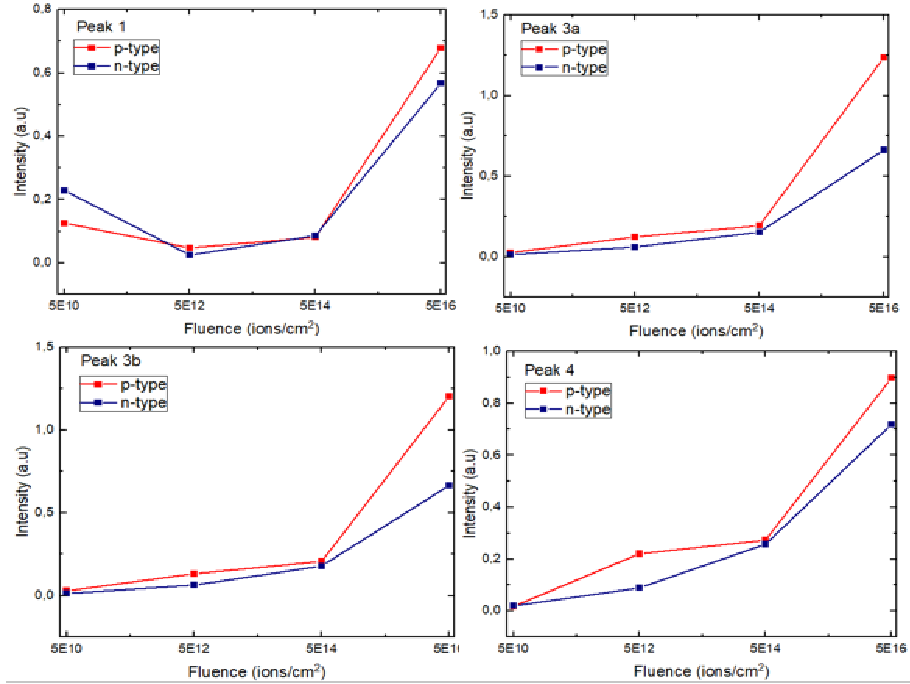

Figure 14.5: Intensity of Peak 1 (1192nm), 3a (1239nm), 3b (1244nm) and 4 (1282 nm) for different fluences

Name	Wavelength (nm)	Defect	Source
1	1192	X-line	[20, 1]
2	1218	W-line	[20, 1]
3a	1239	-	-
3b	1244	W' (phonon replica of W-line)	[20, 1]
4	1282	VO, C_iC_s or G-center	[5, 4] or [17]

Table 14.1: Parameters of the PL peaks illustrated in figure 14.4

Chapter 15

Four Point Measurement

With the use of t = 500μm, the correction factors C1 = 0.6337 and C2 = 4.1712, the four point measurement yielded

$$\rho = 0.6337 \times 4.1712 \times \frac{V}{I} \times 0.05cm \tag{15.1}$$

which gave the resistivity in table 15.1 The results for each sample is an average of three resistivities which were found at three different currents and the average 4-5 voltages these currents yielded. The currents were chosen close to the threshold limit. The four-point measurements took place before removing the natural oxide layer and this is most likely the cause of the obscure results. An additional measurement were made on the p-type after the contact removal, etching, rinsing and drying but it did not yield any big differences in the results magnitude-wise. This may mean that all of the oxide was not removed even though we got some good results from the DLTS measurements. It could also be some other reasons, like a bad wafer since the natural oxide layer should only be a couple of nm, while the etching should have taken away approximately 30 nm.

n-type	Fluence (ions/cm^2)	ρ (Ω-cm)
12	0	5.60
1	5×10^{10}	5.73
2	5×10^{12}	6.33
3	5×10^{14}	86.07
4	5×10^{16}	Not available
p-type		
30	0	5.83
19	5×10^{10}	5.85
20	5×10^{12}	468.34
23	5×10^{14}	72564.89
22	5×10^{16}	Not available

Table 15.1: Proton fluence vs resistivity

Chapter 16

Electrical Characterization

16.1 CV measurements

The capacitance-voltage measurements for n- and p-type silicon samples with fluence 5E10, 5E12 and reference are shown in appendix D figure D.1 and D.2 and their corresponding 1/C^2-V curves are illustrated in figure 16.1 a) and b). The samples with fluences 5E14 and 5E16 are not shown because their

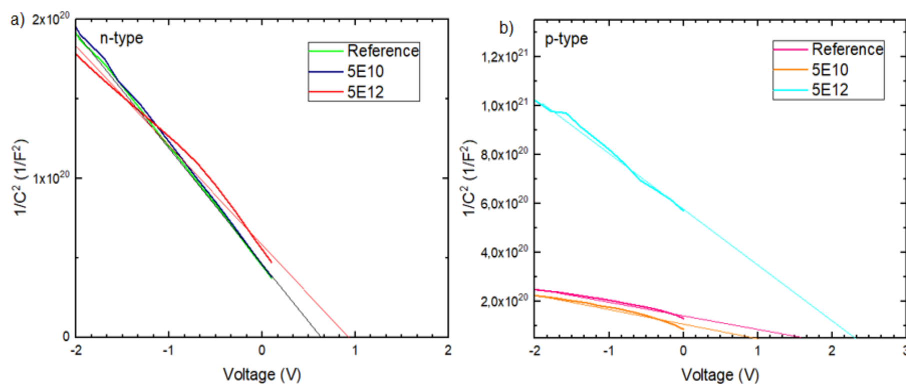

Figure 16.1: Room temperature 1/C^2-V measurements of n- (left) and p-type (right) with reference and the two lowest fluences and extrapolated lines to show built in voltage

capacitance was too low to get any meaningful results. The low capacitance can be explained by large defect concentrations introduced by higher proton fluences, which, next to donors, also creates acceptor-like defects (for n-type). These compensate the charge of free carriers which, from a certain fluence, leaves the semiconductor without any free carriers. The built in voltage is deduced from extrapolated lines of the 1/C^2-V curves. For n-type the built in voltage was $\sim$ 0.7V for the reference and the sample with 5E10 fluence while the 5E12 fluence sample were $\sim$ 0.9V. For p-type the reference were $\sim$ 1.5V, 5E10 $\sim$ 1V and 5E12 $\sim$ 2.3V. Built-in voltages higher than $\sim$ 1/2 of the band gap are highly unlikely and this most likely comes from the weird shape of the doping profiles (i.e them not being spatially homogeneous). The carrier concentrations

for n- and p-type with fluences 5E10, 5E12 and reference illustrates this and are shown in figures 16.2 a) and b), respectively. As seen it is fairly constant in

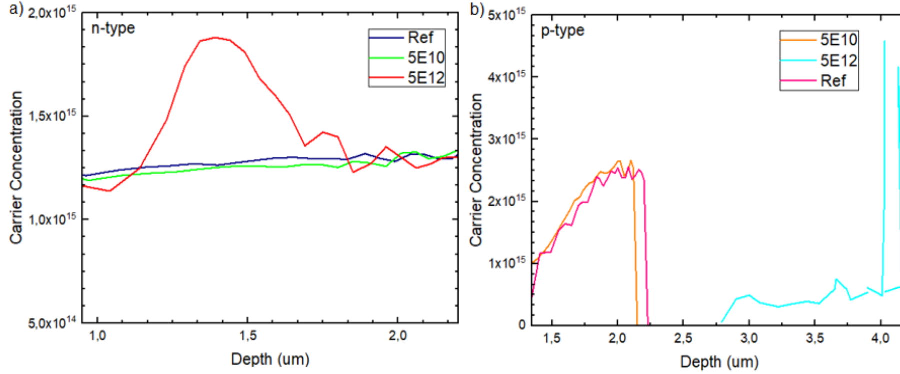

Figure 16.2: Carrier concentration vs depth for n- (left) and p-type (right) with reference and the two lowest fluences

the n-type for the reference and 5E10 fluence, while it varies with depth for the 5E12 sample. This is caused irradiation damage on the crystal structure and for the two higher fluences (5E14 and 5E16), the signal was absent in this range. The p-type carrier concentration is a bit more noisy and the charge carriers in the 5E12 sample is almost compensated as so the DLTS couldn't work. The carrier concentrations are used later in collaboration with the DLTS simulated spectra to give the concentration of various defects.

16.2 DLTS

The DLTS signals for the 640ms window of n- and p-type reference, 5E10 and 5E12 samples are shown in figure 16.3 and 16.4. and this window was chosen because of its relatively low noise. In Appendix E all six rate windows are shown for the 5E12 fluence samples for both n- and p-type to illustrate the shift of the peaks. In figure 16.3 we see that the 5E12 fluence has two distinct peaks of different height, while the 5E10 fluence have some smaller peaks at lower temperatures. From the C-T measurements given in figures 16.7 it is seen that the measurements for the n-type 5E12 sample below 110K must be taken with a pinch of salt since it looks like the carriers are trapped below this temperature. The p-type in figure 16.4 show two large distinct peaks with shoulders on them both which is illustrated when both n- and p-type are analysed in figure 16.5 and 16.6. These figures are simulated peaks by the use of the python tool developed by Christian Zimmermann. Table 16.1 gives the concentration of defects, activation energy, apparent capture cross section and lastly what defect this could be according to the parameters acquired by the simulation tool analysis. The defect concentration was calculated with the aid of the carrier concentration previously obtained and the simulated spectra which has y-axis $N_T/2N_d$. The samples that gave the best results were the 5E12 fluence for both n- and p-type. The large order of magnitude between successive samples made the higher fluences basically useless for this type of analysis. The DLTS signals detected were believed to be mostly intrinsic defects because of the nature of the

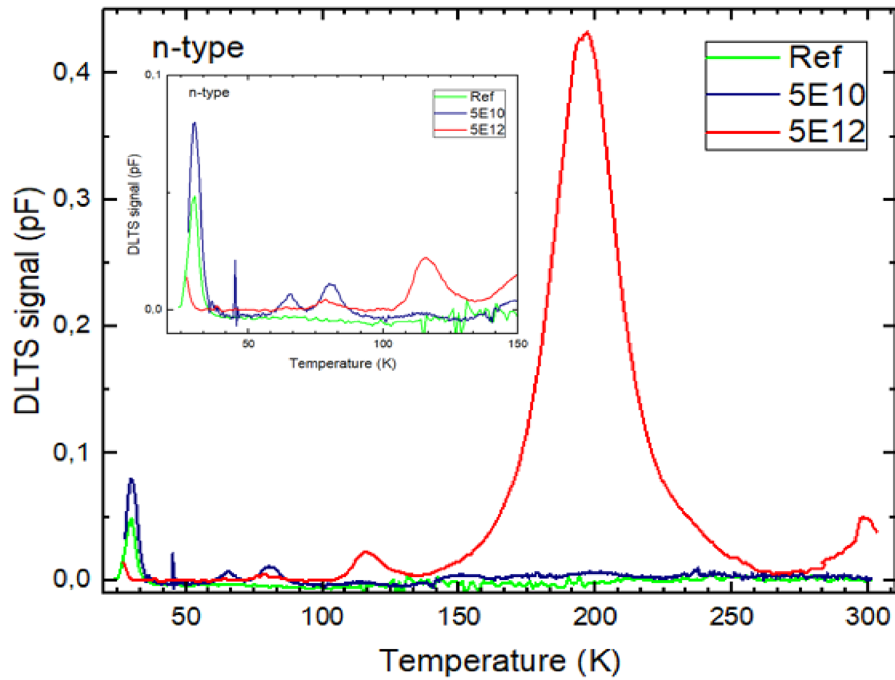

Figure 16.3: DLTS signal vs temperature for n-type with enlarged area in top left to illustrate low temperature peaks

sample treatment and also the activation energies from the analysis matching previous literature.

In n-type silicon the singly (E_c - 0.43 eV) and doubly negative (E_c - 0.24 eV) divacancy (V_2) dominate along with the C_iO_i (E_v + 0.35 eV) and vacancy-oxygen (VO) complex (E_c - 0.18 eV) [5, 25, 32, 4]. The vacancy-phosphorus (VP) center is also present at E_c - 0.43 eV while the carbon interstitial-carbon substitutional (C_iC_s) complex gives a small contribution to the VO peak at E_c - 0.18 eV [4]. Phosphorus forms a complex with carbon (C_iP_s) at E_c - 0.36 eV and also worth mentioning are the two divacancy-oxygen centers (V_2O(0/-) and V_2O(-/=)) at E_c - 0.46 eV and E_c - 0.23 eV, respectively [25, 5].

For p-type we have from the works of Trauwaert and references therein; the divacancy (V_2) at E_v + 0.19 eV, the divacancy-oxygen (V_2O) complex and B_iO_i at E_v + 0.24 eV [3]. At E_v + 0.36 eV the carbon interstitial-oxygen interstitial (C_iO_i) lies while the boron interstitial-carbon substitutional complex (B_iC_s) have position E_v + 0.29 eV. They also reported levels at E_v + 0.26 and 0.29 eV which they thought where multivacancy-oxygen complexes [3] and a midgap level at E_c - 0.54 is believed to be V_3 [5]. From the results of the DLTS measurements for the samples, some peaks are able to be matched.

From figure 16.5 the B (0.18 eV) and F (0.17 eV) peaks are most likely the vacancy-oxygen complex (VO) with some contribution from the carbon interstitial-

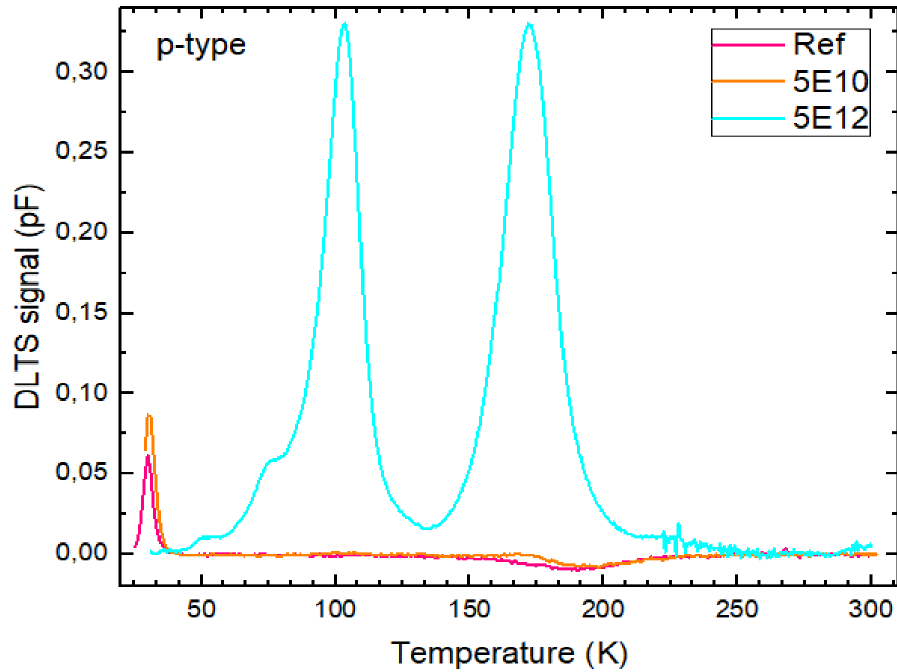

Figure 16.4: DLTS signal vs temperature for p-type

carbon substitutional complex (C_iC_s). The peak named G corresponds to the doubly negative divacancy (V_2(-/=)) while the one named I and D are most likely the singly negative divacancy (V_2(0/-)) with a mixture of the vacancy-phosphorus center. The close proximity in energy to the divacancy-oxygen complexes (0.23 and 0.46 eV) could mean that G, I and D corresponds to them, but since formation of these are more likely during annealing, the other defects were chosen instead. Peak C and H might be related to the carbon interstitial-phosphorus substitutional complex (C_iP_s) while A and E were inconclusive.

For p-type the J peak is attributed to the C_iC_s complex [37]. Both peak L and M in figure 16.6 could be the divacancy according to parameters given in table 16.1 but M is believed to be right because of its larger concentration. The N peak corresponds to the C_iO_i and this could also be what the O peak is because of the large concentration and this defect being one of the most dominant hole traps in p-type silicon [42]. The P peak may be the midgap defect V_3 that Pintilie and Trauwaert mentioned [3, 32]. K and L was inconclusive because of their activation energy not matching literature even though their concentrations are substantial.

The capacitance vs temperature measurements are shown in 16.7 a) and b) for n- and p-type, respectively. The bias over the temperature range were -5V and as seen in n-type the freeze out occurs at around 110K for the 5E12 fluence. This is caused by the compensating defects created which "eat" free carriers. For the p-type 5E12, the capacitance varies with temperature as expected for

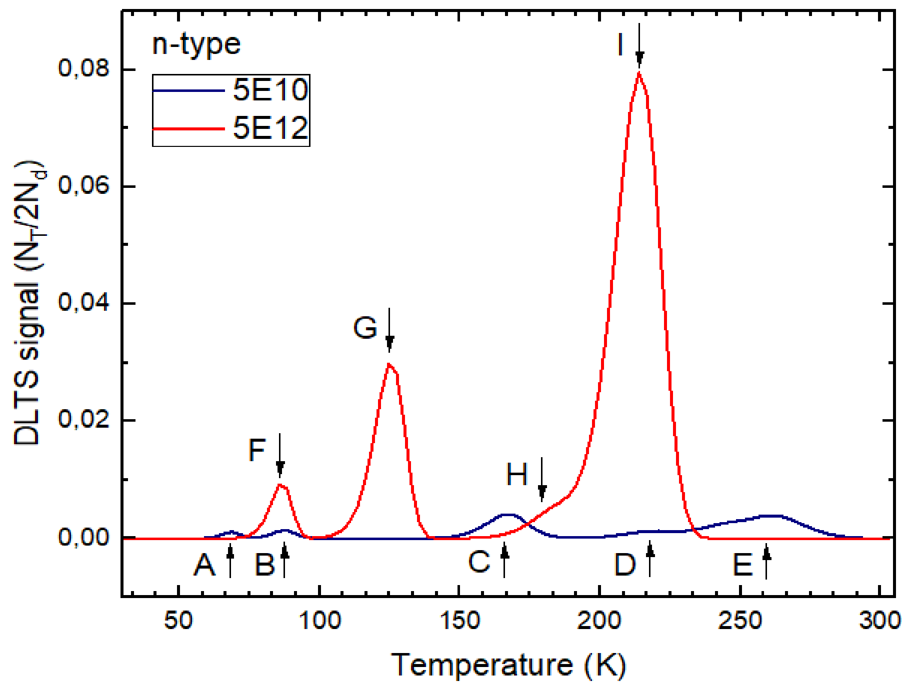

Figure 16.5: Simulated DLTS spectrum for n-type with fluence 5E12

defects but the freeze-out happens at much lower temperatures than for n-type. There is some small variances in the lower fluences as well and the concentration of these defects is thereby very low.

The energies for the emission peaks of the PL results and the activation energies of the defects in the DLTS analysis are compared in figure 16.8 for n-type. From this we are able to match some of the results like the P-line of the PL measurements corresponds to the signal from peak C from figure 16.5 which from literature is attributed to the carbon-interstitial-phosphorous substitutional (C_iP_s) complex [25]. It is tempting to then assign the P-line to this defect but the intensity of the P-line vs fluence for both n- and p-type in figure 14.2 b) does not vary much from n- to p-type and the p-type intensity are even greater than the n-type for most fluences. This makes it unlikely that this phosphorous complex (C_iP_s) is the P-line . The energy of C-line being in close proximity to the DLTS peak "H" means that this peak may also be attributed to to the C_iO_i complex [34]. The PL and DLTS results for p-type are depicted in figure 16.9 and the previously inconclusive DLTS peak named "K" is matched with the energy of the W-line. Also seen is a match between the C-line and the "N" peak which both have been assigned the C_iO_i complex from literature [34, 42]. The DLTS "J" peak is credited to the C_iC_s in literature [37] while the close proximity PL "1" peak is the X-line (complex cluster of interstitial silicon) in literature [20, 1]. This may mean the actual structure of the X-line have been found and is believed to be the C_iC_s complex.

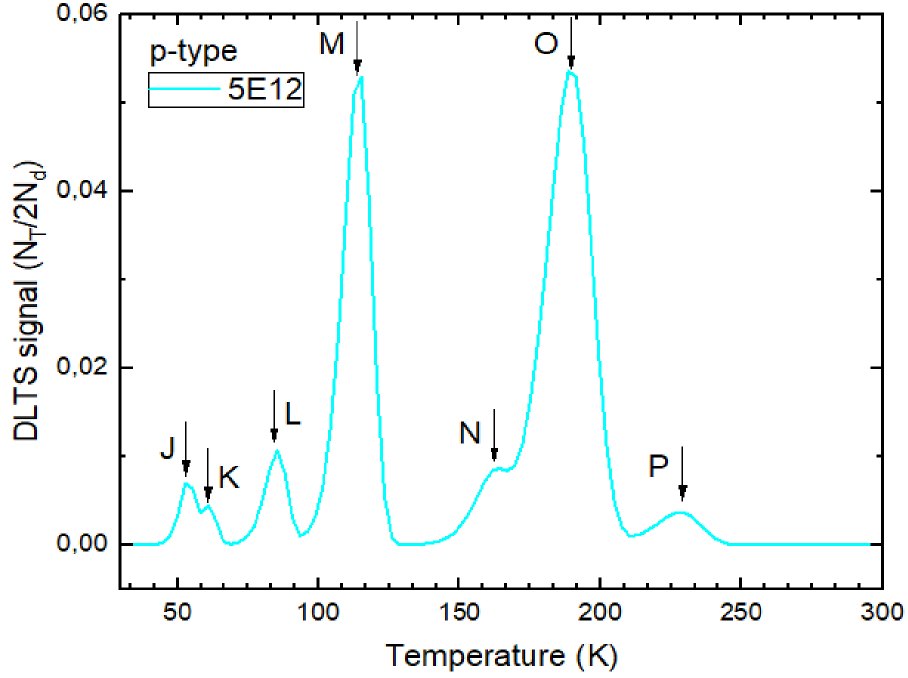

Figure 16.6: Simulated DLTS spectrum for p-type with fluence 5E12

n-type	N_T (defects/cm^3)	E_a (eV)	σ_a (cm^2)	Defect	Source
A	2.824×10^{12}	0.13	3.33×10^{-19}	-	
B	3.588×10^{12}	0.18	1.64×10^{-18}	VO, C_iC_s	[5, 4]
C	1.061×10^{13}	0.35	1.00×10^{-18}	C_iP_s	[25]
D	3.051×10^{12}	0.47	9.25×10^{-19}	V_2(0/-), VP	[5, 4]
E	1.008×10^{13}	0.61	4.17×10^{-17}	-	
F	2.373×10^{13}	0.17	3.14×10^{-18}	VO, C_iC_s	[5, 4]
G	7.747×10^{13}	0.25	1.43×10^{-18}	V_2(-/=)	[5]
H	1.184×10^{13}	0.38	2.10×10^{-18}	C_iP_s or C_iO_i	[25, 34]
I	2.066×10^{14}	0.48	8.28×10^{-18}	V_2(0/-), VP	[5]
p-type					
J	4.884×10^{12}	0.09	3.33×10^{-19}	C_iC_s	[37]
K	3.116×10^{12}	0.12	3.37×10^{-18}	W-line	Fig 16.12
L	7.487×10^{12}	0.16	1.00×10^{-18}	-	
M	3.706×10^{13}	0.22	9.25×10^{-19}	V_2	[3]
N	6.070×10^{12}	0.38	5.44×10^{-17}	C_iO_i or C_iO_{2i}	[42] or [35]
O	3.752×10^{13}	0.39	7.21×10^{-19}	C_iO_i or C_iO_{2i}	[42] or [35]
P	2.590×10^{12}	0.56	9.09×10^{-17}	V_3	[3, 32]

Table 16.1: DLTS simulated parameters for defects

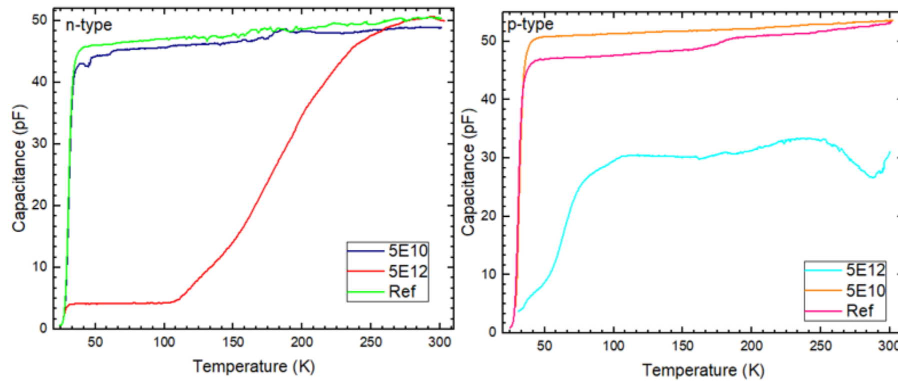

Figure 16.7: CT measurements of n- (left) and p-type (right) with reference and the two lowest fluences with bias -5V

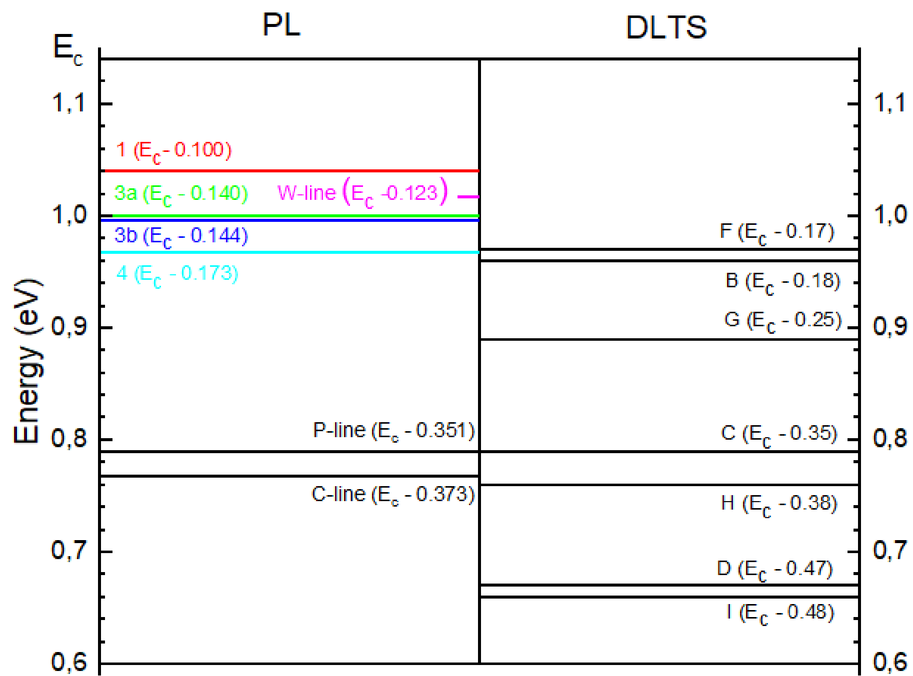

Figure 16.8: Schematic of different energy levels from PL and DLTS for n-type

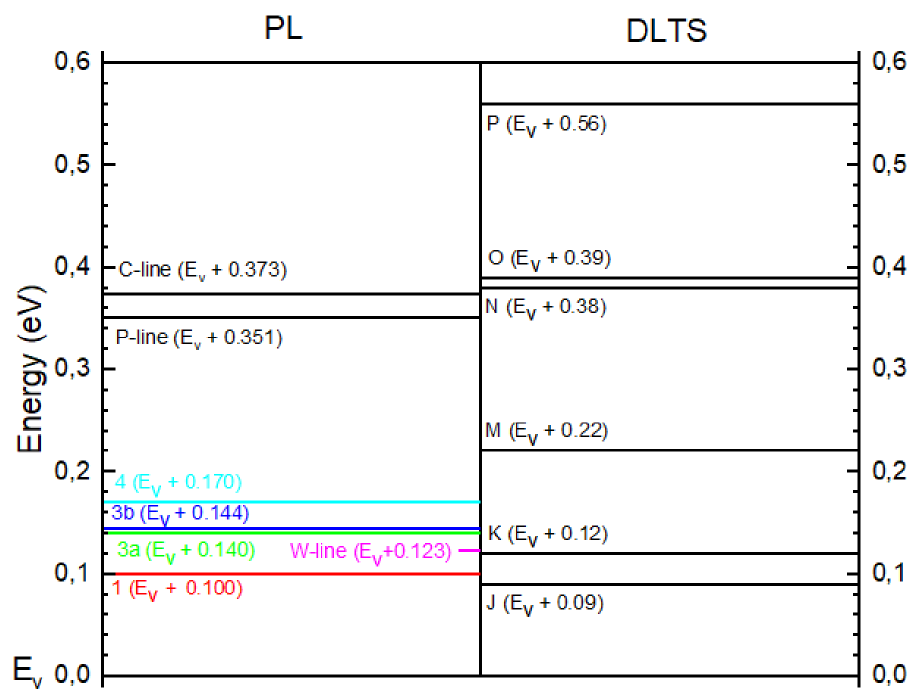

Figure 16.9: Schematic of different energy levels from PL and DLTS for p-type

Part V

Conclusion and Future Work

Chapter 17

Conclusion

This thesis tried to deal with identifying the defects of some of the previously discovered single-photon sources in silicon by means of photoluminescence spectroscopy and deep level transient spectroscopy. Samples of both n- and p-type CZ Si were irradiated with 1.8 MeV protons in a range of fluences from 5E10 to 5E16 to create defect structures that could correspond to said single-photon sources. Cryogenic condition (4K) PL was used to identify the irradiation-induced defects in the samples and to see trends from fluence dependencies on the intensity of the measured spectra. For the electrical characterization, DLTS was employed to identify different energy levels of the defects and thereby the nature of their origin. Then the information from both the PL and DLTS experiments were compared to get the best analysis of the defects as possible.

The proton irradiation technique used in this work were unable to reproduce the peaks that proved to be single photon emitters for Durand et al. The most probable reason is that the previous experiment also used carbon for their irradiation. Our results however, did give some distinct peaks in the telecom range that could prove to be SPEs since sharp peaks are a sign of single-photon emission. Some of the most promising peaks found were the X-line (1192nm), the W-line (1218nm) and "4" (1282nm). The literature suggest the W-line and X-line originate from competing differently sized complex clusters of interstitial silicon. The way their intensities could be manipulated in accordance to fluence further back this claim with the highest fluence giving the greatest intensities. By comparing the spectra of both PL and DLTS measurements, peak "4" was found to be the vacancy-oxygen complex (VO) with some contribution from the carbon interstitial-carbon substitutional complex (C_iC_s). Its close proximity to the G-line might mean that it is in fact this well-known single-photon emitter instead or that the G center contributes to "4"s intensity. The previously unknown interstital silicon cluster, the X-line, is from comparison of PL and DLTS energies found to be attributed to the C_iC_s complex as well, even though PL literature has it as a complex cluster of silicon. The way the intensity of the X-line evolves, it is difficult to say for sure which is right, but I am leaning on the fluence dependency and saying still that it is a complex cluster of interstitial silicon.

Chapter 18

Future Work

The future of silicon as a single-photon source for quantum technology looks promising but there are still obstacles that must be handled. First of all the emitters must be in the appropriate range in accordance to their intended use (telecommunication, computing, etc.). Then the optically active defects must be identified and verified to be single-photon sources of high quality as purity and indistinguishability will be important for certain technologies. The process of an easy on-demand production of these defects must be in place before scalable solutions for quantum technology are established.

In the present study, identification of several promising peaks that may turn out to be single-photon emitters were found. The most hopeful are the X-line at 1192nm, W-line at 1218nm and peak "4" at 1282nm. It is necessary to study the single-photon purity of the observed PL peaks by photon correlation experiments in order to identify which are single-photon emitter ($g^2(0) < 0.5$). The experiments that allow this kind of study is the HBT interferometer, which is currently under development at the University of Oslo. Afterward, a detailed study of photon purity as a function of oxygen and carbon concentration would be a fundamental step to on-demand silicon single-photon sources.

Appendix A

Photon Statistics I - Quantized Electric field and Operator Notion

Appendix B is based on Stevens [38]. The quantized electric field can be written as an operator

$$\hat{E}(\vec{r},t) = \sum_j [\hat{E}_j^{(+)}(\vec{r},t) + \hat{E}_j^{(-)}(\vec{r},t)] \tag{A.1}$$

where $\hat{E}_j^{(+)}$ and $\hat{E}_j^{(-)}$ represents the positive and negative frequency components of the field in mode j. The modes j have some specific spatial extent, propagation vector, wavelength, polarization, spectral and temporal profiles. The frequency components are related through

$$\hat{E}_j^{(-)}(\vec{r},t) = [\hat{E}_j^{(+)}(\vec{r},t)]^\dagger \tag{A.2}$$

where † is the Hermitian conjugate. The electromagnetic field can be treated as a quantized harmonic oscillator with

$$\hat{H} = \sum_j \hbar\omega_j \left(\hat{a}_j^\dagger \hat{a}_j + \frac{1}{2}\right) \tag{A.3}$$

where $\hat{H}$ is the Hamiltonian and $\hat{a}_j^\dagger$ is the creation operator and signify the addition of a photon to mode j

$$\hat{a}_j^\dagger |n\rangle_j = \sqrt{n+1}|n+1\rangle_j \tag{A.4}$$

$|n\rangle_j$ is the photon number state and denotes photons in mode j. The annihilation operator, $\hat{a}_j$, signify removal of a photon from mode j

$$\hat{a}_j |n\rangle_j = \sqrt{n}|n-1\rangle_j \tag{A.5}$$

The number states and the creation and annihilation operator are correlated through the number operator $\hat{n}_j$, with the number states being eigenstates of the number operator

$$\hat{n}_j |n\rangle_j = \hat{a}_j^\dagger \hat{a}_j |n\rangle_j = n|n\rangle_j \tag{A.6}$$

The positive-frequency component of the quantized electromagnetic field for a monochromatic light can be written as

$$\hat{E}_j^{(+)}(\vec{r},t) = \varepsilon_j \vec{e}_j \hat{a}_j e^{i(k_j \cdot \vec{r} - \omega_j t)} \tag{A.7}$$

where ω_j is the angular frequency, k_j the wavevector, $\vec{e}_j$ the unit vector describing the polarization and ε_j=i$\sqrt{\hbar\omega_j/2\epsilon_0 V}$, where V is the volume of the mode. For fields that are not monochromatic, changes to equation B.7 must be made.

Appendix B

Photon Statistics II - Second-Order Coherence, $g^{(2)}$

Appendix C is based on Stevens [38]. The second order coherence, $g^{(2)}$, is one of the most common measurement methods to determine if the source is a single-photon emitter. It gives information about the probability of multi-photon emission from a source. $g^{(2)}$ between two modes j and k, measured at position $\vec{r}_1$ and time t_1 and position $\vec{r}_2$ and time t_2, respectively, is given by

$$g^{(2)}_{j,k}(\vec{r}_1, t_1; \vec{r}_2, t_2) = \frac{\langle \hat{E}^{(-)}_j(\vec{r}_1, t_1)\hat{E}^{(-)}_k(\vec{r}_2, t_2)\hat{E}^{(+)}_k(\vec{r}_2, t_2)\hat{E}^{(+)}_j(\vec{r}_1, t_1)\rangle}{\langle \hat{E}^{(-)}_j(\vec{r}_1, t_1)\hat{E}^{(+)}_j(\vec{r}_1, t_1)\rangle\langle \hat{E}^{(-)}_k(\vec{r}_2, t_2)\hat{E}^{(+)}_k(\vec{r}_2, t_2)\rangle} \tag{B.1}$$

rewriting in terms of the creation and annihilation operators gives

$$g^{(2)}_{j,k}(\vec{r}_1, t_1; \vec{r}_2, t_2) = \frac{\langle \hat{a}^\dagger_j(\vec{r}_1, t_1)\hat{a}^\dagger_k(\vec{r}_2, t_2)\hat{a}_k(\vec{r}_2, t_2)\hat{a}_j(\vec{r}_1, t_1)\rangle}{\langle \hat{a}^\dagger_j(\vec{r}_1, t_1)\hat{a}_j(\vec{r}_1, t_1)\rangle\langle \hat{a}^\dagger_k(\vec{r}_2, t_2)\hat{a}_k(\vec{r}_2, t_2)\rangle} \tag{B.2}$$

This can be simplified for a single-mode (j=k), stationary source (properties depend on time delay and not t_1 and t_2) measured at positions considered equal ($\vec{r}_1$=$\vec{r}_2$)

$$g^{(2)}(\tau) = \frac{\langle \hat{a}^\dagger(t)\hat{a}^\dagger(t+\tau)\hat{a}(t+\tau)\hat{a}(t)\rangle}{\langle \hat{a}^\dagger(t)\hat{a}(t)\rangle^2} \tag{B.3}$$

$\tau = 0$ is frequently used for characterizing single-photon emitters and this yields

$$g^{(2)}(0) = \frac{\langle \hat{n}(t)(\hat{n}(t) - 1)\rangle}{\langle \hat{n}(t)\rangle^2} \tag{B.4}$$

The second order coherence can be related to the probability of emission of one or more photons for both pulsed and continuous-wave sources.

Appendix C

PL spectra

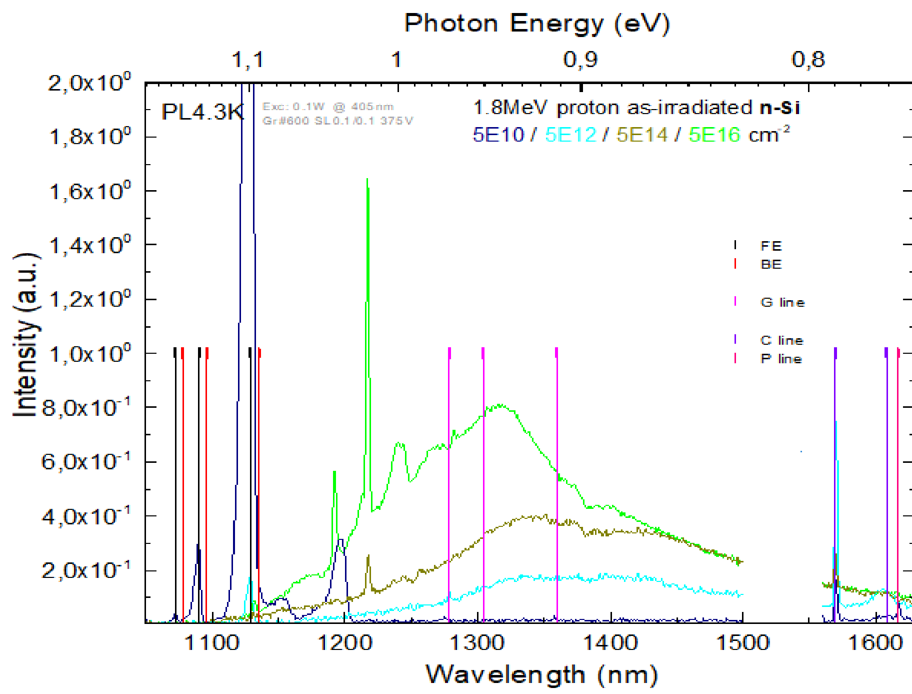

Figure C.1: PL spectra of n-type silicon in linear scale

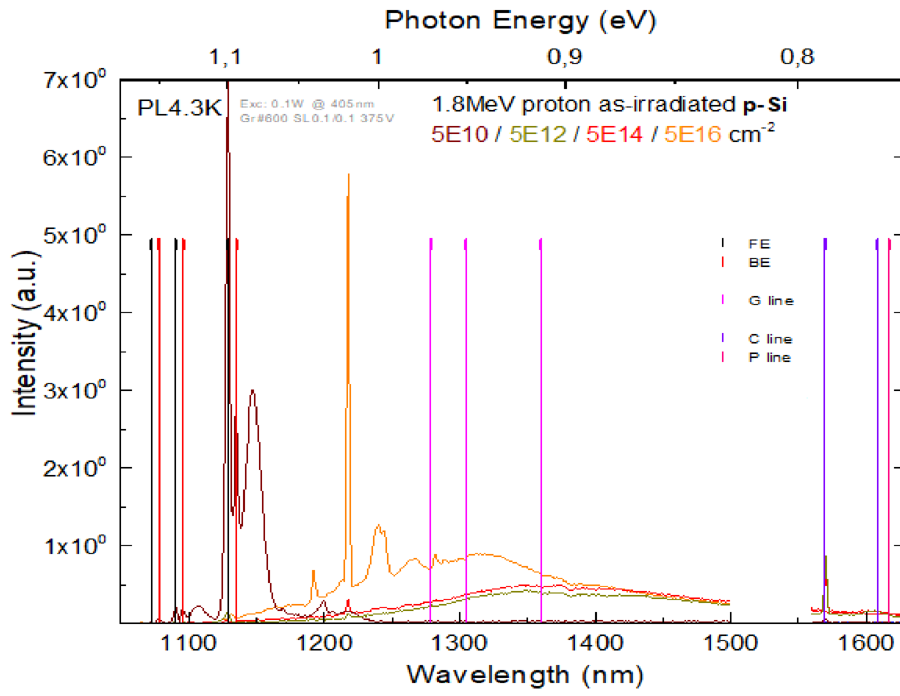

Figure C.2: PL spectra of p-type silicon in linear scale

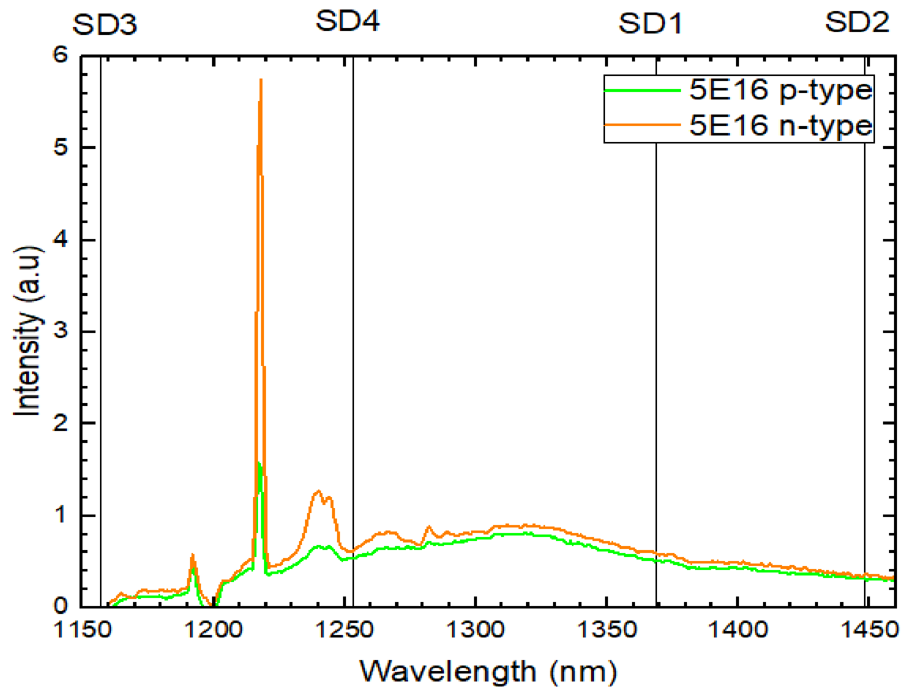

Figure C.3: PL spectra n- and p-type 5E16 fluence with SD1-SD4 marked

Appendix D

CV measurements

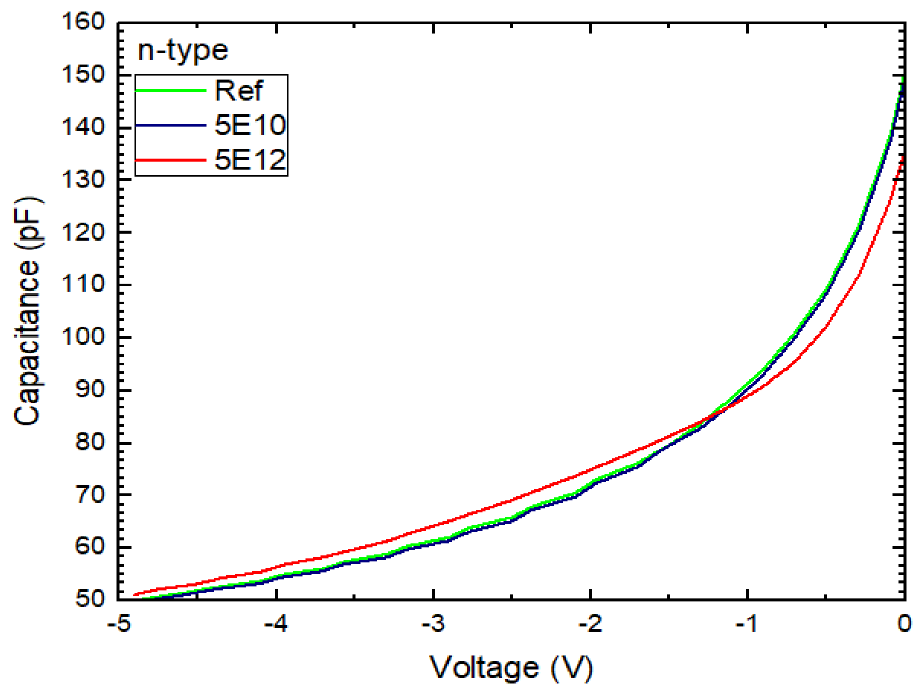

Figure D.1: Room temperature CV measurements of n-type with reference and the two lowest fluences

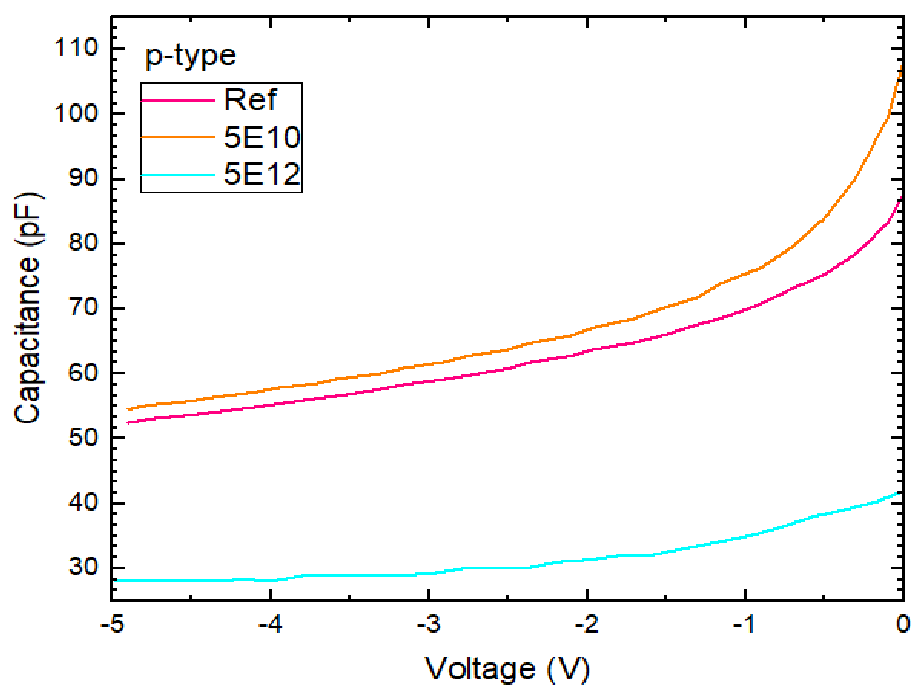

Figure D.2: Room temperature CV measurements of p-type with reference and the two lowest fluences

Appendix E

Rate Windows

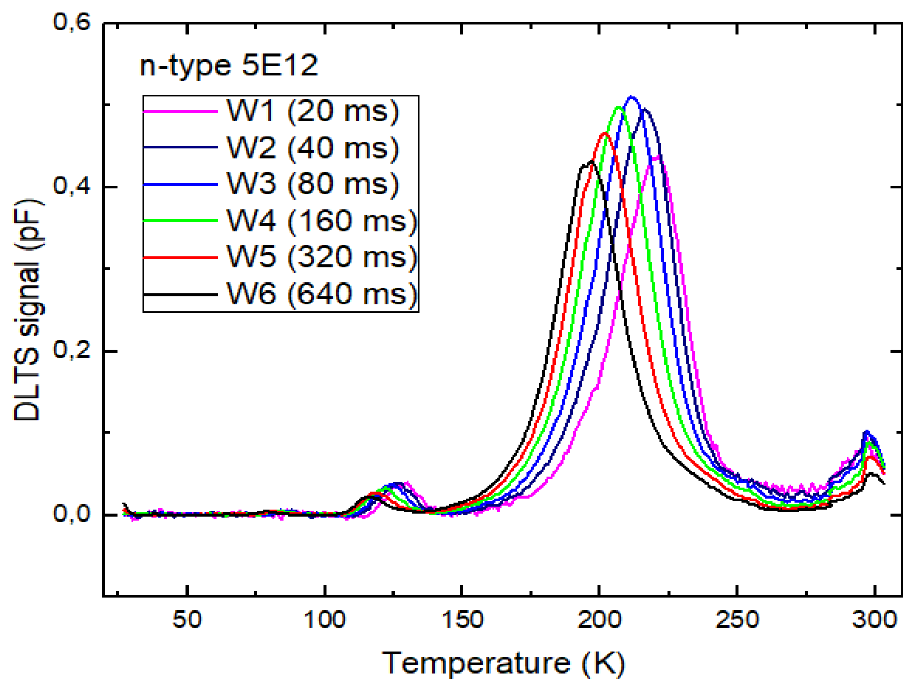

Figure E.1: The six different rate windows for the n-type 5E12 fluence sample

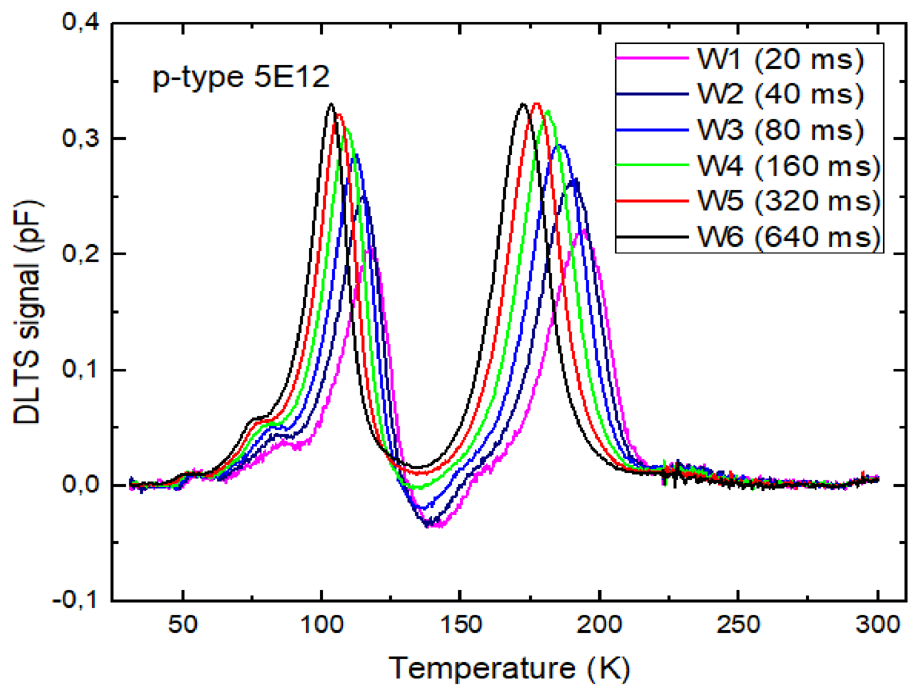

Figure E.2: The six different rate windows for the p-type 5E12 fluence sample

Bibliography

[1] Maria Aboy et al. "W and X Photoluminescence Centers in Crystalline Si: Chasing Candidates at Atomic Level Through Multiscale Simulations". In: *Journal of ELECTRONIC MATERIALS* 47 (9 2018). DOI: https://doi.org/10.1007/s11664-018-6300-z.

[2] Igor Aharonovich, Dirk Englund, and Miles Toth. "Solid-state single-photon emitters". In: *Nature Photon* 10 (2016), pp. 631–641. DOI: https://doi.org/10.1038/nphoton.2016.186.

[3] M.A Trauweart et al. "Low-temperature anneal of the divacancy in p-type silicon: A transformation from V2 to VxOy complexes?" In: *Applied Physics Letters* (1995). DOI: DOI:10.1063/1.114276.

[4] P. Pellegrino et al. "Annealing kinetics of vacancy-related defects in low-dose MeV self-ion-implanted n-type silicon". In: *PHYSICAL REVIEW B* 64 (2001). DOI: 10.1103/PhysRevB.64.195211.

[5] G Alfieri et al. "Evidence for identification of the divacancy-oxygen center in Si". In: *Physical Review B* 63 (2003), pp. 21–24. DOI: 10.1103/PhysRevB.68.233202.

[6] Alain Aspect and Philippe Grangier. *The First Single Photon Sources and Single Photon Interference Experiments.* 2019.

[7] M Auslender and S. Hava. *Single-Crystal Silicon: Electrical and Optical Properties.* Springer, 2017. ISBN: 978-3-319-48933-9. DOI: https://doi-org.ezproxy.uio.no/10.1007/978-3-319-48933-9_21.

[8] Marianne Etzelmüller Bathen. "Point defects in silicon carbide for quantum technologies: Identification, tuning and control". Philosophiae Doctor. University of Oslo, 2020.

[9] Marianne Bathen, Robert Karsthof, and Julie Bonkerud. *DLTS Setup IDEFIX.* 2020.

[10] J.C Bienfang et al. "Introduction". In: *Academic Press* 45 (2013), pp. 1–24. DOI: https://doi.org/10.1016/B978-0-12-387695-9.00001-9.

[11] Sonia M. Buckley et al. "Optimization of photoluminescence from W centers in silicon-on-insulator". In: *Opt. Express* 28 (11 2020), pp. 16057–16072. DOI: https://doi.org/10.1364/OE.386450.

[12] I Buyanova et al. "Photoluminescence characterization of defects created in electron-irradiated silicon at elevated temperatures". In: *Material Science and Engineering* 72 (2000), pp. 146–149. DOI: 10.1016/S0921-5107(99)00491-2.

[13] Michel Che and Jacques Vedrine. *Characterization of Solid Materials and Heterogeneous Catalysts: From Structure to Surface Reactivity*. Wiley, 2015, pp. 149–184. ISBN: 9783527645329.

[14] Gordon Davies. "The optical properties of luminescence centres in silicon". In: *Physics Reports* 176 (3-4 1989), pp. 83–188. DOI: //doi.org/10.1016/0370-1573(89)90064-1.

[15] David P DiVicenzo. "The Physical Implementation of Quantum Computation". In: *Fortschritte Der Physik* 48 (2000), pp. 771–783.

[16] Cyrus E Dreyer et al. "First-Principles Calculations of Point Defects for Quantum Technologies". In: *Annual Review of Materials Research* 48 (1 2018), pp. 1–26. DOI: 10.1146/annurev-matsci-070317-124453.

[17] A. Durand et al. "Broad Diversity of Near-Infrared Single-Photon Emitters in Silicon". In: *Phys. Rev. Lett.* 126 (8 Feb. 2021), p. 083602. DOI: 10.1103/PhysRevLett.126.083602. URL: https://link.aps.org/doi/10.1103/PhysRevLett.126.083602.

[18] Dilla Duryha Berhanuddin. "Generation and characterisation of the carbon G-centre in silicon". Philosophiae Doctor. University of Surrey, 2015.

[19] Franziska Fuchs. "Optical spectroscopy on silicon vacancy defects in silicon carbide". Philosophiae Doctor. Julius-Maximilians University, 2015.

[20] Pravat Giri. "Photoluminescence signature of silicon interstitial cluster evolution from compact to extended structures in ion-implanted silicon". In: *Semiconductor Science and Technology* 20 (2005), p. 638. DOI: 10.1088/0268-1242/20/6/027.

[21] David J. Griffiths. *Introduction to Quantum Physics*. Cambridge University Press, 2017.

[22] Friedemann D. Heinz. *Microscopic Photoluminescence Spectroscopy on Silicon*. Fraunhofer Verlag, 2017. ISBN: 978-3-8396-1099-2.

[23] Charles Kittel. *Introduction to Solid State Physics*. 8th Edition. Wiley, 2005. ISBN: 978-0-471-41526-8.

[24] Jordan McEwen. *Jablonski diagram*. URL: https://chem.libretexts.org/Bookshelves/Physical_and_Theoretical_Chemistry_Textbook_Maps/Supplemental_Modules_(Physical_and_Theoretical_Chemistry)/Spectroscopy/Electronic_Spectroscopy/Jablonski_diagram.

[25] E.V Monakhov et al. "Formation of a double acceptor center during divacancy annealing in low-doped high-purity oxygenated Si". In: *Physical Review B* 65 (2002), pp. 71–74. DOI: 10.1103/PhysRevB.65.233207.

[26] G. E. Moore. In: *Electronics* 38 (1965).

[27] Minoru Nakamura and Siro Nagai. "Influence of high-energy electron irradiation on the formation and annihilation of the photoluminescence W center and the center's origin in a proton-implanted silicon crystal". In: *Phys. Rev. B* 66 (2002). DOI: 10.1103/PhysRevB.66.155204.

[28] Jenny Nelson. *The Physics of Solar Cells*. Imperial Collage Press, 2003. ISBN: 1-86094-349-7.

[29] Truls Nordby. *Defects and Transport in Crystalline Materials*. 2015.

[30] Jeremy L. O'Brien. "Optical Quantum Computing". In: *Science (American Association for the Advancement of Science)* 318 (5856 2007), pp. 1567–1570. DOI: 10.1126/science.1142892.

[31] Paolo Pellegrino. "Point Defects in Ion-Implanted Silicon and Silicon Carbide". Teknisk Doktor (PhD). Kungliga Tekniska Høgskolan, 2001.

[32] I Pintilie. "Second-order generation of point defects in gamma-irradiated float-zone silicon, an explanation for "type inversion"". In: *APPLIED PHYSICS LETTERS* 82.13 (2003). DOI: https://doi.org/10.1063/1.1564869.

[33] Hartmut Pohl. *What is the difference between fluorescence, phosphorescence and luminescence?* URL: https://www.enzolifesciences.com/science-center/technotes/2019/december/what-is-the-difference-between-fluorescence-phosphorescence-and-luminescence?/.

[34] Bahman Raeissi et al. "PL and DLTS Analysis of Carbon-Related Centers in Irradiated p-Type Cz-Si". In: *Solid State Phenomena* 105-206 (2013), pp. 224–227. DOI: https://doi.org/10.4028/www.scientific.net/SSP.205-206.224.

[35] Bahman Raeissi et al. "PL and DLTS analysis of carbon–related centers in irradiated p–type Cz–Si ". In: *Solid State Phenomena* 205-206 (2013). DOI: https://doi.org/10.4028/www.scientific.net/SSP.205-206.224.

[36] Jai Singh. *Optical Properties of Materials and Their Applications*. 2nd Edition. Wiley, 2019, pp. 157–202. ISBN: 9781119506003.

[37] L.W Song et al. "Bistable interstitial-carbon —substitutional-carbon pair in silicon". In: *PHYSICAL REVIEW B* 42.9 (1990), pp. 5765–5783. DOI: 10.1103/PhysRevB.42.5765.

[38] Martin J. Stevens. "Photon Statistics, Measurements, and Measurements Tools". In: *Academic Press* 45 (2013), pp. 25–68. DOI: https://doi.org/10.1016/B978-0-12-387695-9.00002-0.

[39] Ben G Streetman and Sanjay Kumar Banerjee. *Solid State Electronic Devices*. Pearson, 2015. ISBN: 1-292-06055-7.

[40] Richard J. D. Tilley. *Understanding Solids*. 2nd Edition. The Science of Materials. Wiley, 2013. ISBN: 978-1-118-42346-2.

[41] Lasse Vines. "Fundamental Defect Complexes and Nanostructuring of Silicon by Ion Beams". Dissertation for the degree of PhD. University of Oslo, 2008.

[42] Lasse Vines et al. "Formation and origin of the dominating electron trap in irradiated p-type silicon". In: *PHYSICAL REVIEW B* 78.8 (2008). DOI: 10.1103/PHYSREVB.78.085205.

[43] Deren Yang. *Handbook of Photovoltaic Silicon*. Springer, 2019, pp. 397–636.

[44] Yutaka Yoshida and Guido Langouche. *Defects and Impurities in Silicon Materials*. Springer, 2016. ISBN: 9784431557999.